Numerical prediction of erosion in a choke valve

by
Lise Margrethe Rinde

Master of Science Thesis in
Process Technology

Department of Physics and Technology
University of Bergen

May 2019

Acknowledgments

First and foremost I would like to thank Sigurd Gaard and Florian Leopold at Wintershall Norge AS for the opportunity to write a thesis for them. They have been very cooperative and provided important and evident material to complete this thesis.

Furthermore, I would like to express my gratitude towards my supervisor Prof. Pawel Jan Kosinski and co-supervisor Prof. Boris Balakin. Their positive and curious mindset has been very helpful. Moreover, their experience and knowledge about STAR-CCM+ have been crucial. I am thankful for every meeting and the knowledge they have given.

Finally, I would like to thank my fellow students, Halvard Thon, and Jørgen Skivenesvåg, that I could share ideas and laughs with during the time writing my thesis.

Abstract

Erosion wear in pipelines due to multiphase flows is a well-known problem in the petroleum production and transport industries. There are several different ways to predict the erosion damage on the system investigated. Nevertheless, there are very few studies of erosion on choke valves and it is still unclear which models should be selected. Different geometries give different flow profiles and therefore different erosion patterns. Knowledge of where and what magnitude the erosion wear occurs is crucial to obtain efficient and economical production and choke valve design.

In this research, computational fluid dynamics (CFD) with the Lagrangian modeling methodology, was used to examine the erosion wear on a choke valve in a pipeline. The first part of this thesis focused on finding the best-suited erosion wear model for the system. Furthermore, analysis of the impact of particle size and rebound coefficients was performed for the best-suited erosion models. To predict erosion wear using CFD analysis there are three main steps: flow modeling, particle tracking and calculating the erosion wear from the particle interactions.

Nomenclature

Abbreviations

CFD	Computational Fluid Dynamics
CFL	Courant number
CS	Carbon steel
DEM	Discrete element method
DNV	Det Norske Veritas
DPM	Discrete particle method
E-E	Eulerian-Eulerian
E-L	Eulerian-Lagrangian
E/CRC	Erosion/Corrosion Research Center
HC	Hydrocarbon
P-P	Particle-particle
PVT	Pressure volume temperature
RANS	Reynold-averaged Navier-Stokes
RSM	Reynolds stress model
SEM	Scanning electron microscopy
SS	Stainless Steel
T-F	Two-fluid
UT	Ultrasonic testing
V-H	Vertical orientated inlet and horizontal outlet

Greek Symbols

α	Angle in degrees	[-]
$\alpha_{a,b}$	Kinetic energy correction factor at the station a and b	[-]
κ	Thermal conductivity	[W/m-K]
μ	Dynamic viscosity	[Pa-s]
ρ	Density	[kg/m^3]

τ^t	Turbulent stress tensor working on the fluid element	[Pa]
τ_w	Wall shear stress	[Pa]
θ	Angle in radians	[-]

Latin Letters

$\bar{V}$	Average velocity	[m/s]
$\dot{p}$	Particle flow rate	[s^{-1}]
a	Abrasive wear coefficient	[kg/J]
BH	Brinell hardness	[N/m^2]
C	Inter-particle spacing	[m]
c	Specific heat capacity	[J/kg-K]
C_D	Drag coefficient	[-]
D	Diameter of tube	[m]
D_1	Diameter at inlet	[m]
D_2	Diameter at outlet	[m]
d_p	Particle diameter	[m]
d_{ref}	Reference diameter	[m]
e	restitution coefficient	[-]
E_{90}	Reference erosion ratio at 90°	[kg/h]
ER	Erosion rate	[kg/h]
ER_C	Erosion wear from cutting	[kg/h]
ER_D	Erosion wear from deformation	[kg/h]
f	Friction factor	[-]
F_D	Drag force	[N]
F_G	Gravity and buoyancy forces	[N]
F_P	Pressure gradient force	[N]
F_S	Particle shape factor	[-]
F_V	Virtual mass force	[N]
g	Gravity	[m/s^2]
h_f	Total friction generated by fluid	[m^2/s^2]
H_p	Erodent particle hardness	[N/m^2]
H_t	Material hardness	[N/m^2]
H_V	Hardness Vickers	[N/m^2]
K_c	Contraction loss coefficient	[-]
K_e	Expansion loss coefficient	[-]

K_f	Fitting and valve loss coefficient	[-]
L	Length of pipe	[m]
Mw	Molecular weight	[g/mole]
N	Number of moles	[mole]
P	Pressure	[Pa]
R	Universal gas constant	[J/mole-K]
Re	Reynolds number	[-]
S	Cross-sectional area	[m^2]
s	Sliding distance	[m]
S_0	Vena contracta	[m^2]
T	Temperature	[K]
t	Time	[s]
u^*	Reference velocity	[m/s]
V	Volume	[m^3]
v	Kinematic viscosity	[m^2/s]
V_g	Velocity of gas	[m/s]
V_L	Particle impact velocity	[m/s]
v_{ref}	Reference velocity	[m/s]
y	Normal distance from wall to wall-cell centroid	[m]
y^+	Non-dimensional wall distance	[-]

Subscript

a	Given point at the inlet
b	Given point at the outlet
f	Fluid
n	Normal
p	Particle
t	Tangential

Contents

List of Figures

List of Tables

Chapter 1

Introduction

An introduction to background, motivation, and objectives for this thesis.

1.1 Background and motivation

Choke valves in pipelines are ubiquitous in many engineering processes. On the other hand, the conveyance of particles in a flow through chokes causes erosive wear of the structure material. Therefore, to prevent equipment failure, the components have to be replaced frequently. In the oil and gas industry, during well cleanup drilling debris and completion fluids come out of the pipeline causing higher erosion rates than under normal production. Some of this debris does not come up during the clean-up operations and could pose problems, such as higher erosion, during normal production.

Erosion is a well-known problem in the oil industry. Due to collision of solid particles along the pipeline structure, small fragments of the walls can be torn off. Velocity and impact angle of the particles are some of the key parameters in erosion damage. Several researchers have found erosion correlations for different materials and shapes. This thesis also surveys four selected erosion models and particle-wall rebound models and compare them to experiments done on 90 degrees elbows. However, there are very few papers and little research done on erosion wear of choke valves using computational fluid dynamics (CFD). This thesis compares four different erosion models, and particle sizes to investigate the erosion wear.

1.2 Objective

The objective for this thesis was to run CFD simulations with the purpose to numerically investigate the erosion damage on a choke valve during normal production with sand particles, using the simulation software STAR-CCM+.

To achieve an accurate estimation of the erosion, the geometry and fluid data was provided by Wintershall Norge AS. The mathematical models were chosen to best suit the calculations to get the most accurate results. First, the geometry was made in CAD-3D, a modeling tool. Afterward, the erosion was investigated numerically; the mathematical models are shown in detail in Chapter

4. By testing several erosion models and particle-wall rebound models the optimal erosion wear model for the process of gas-solid multiphase system can be found.

Chapter 2

Theory

To get a better understanding of the thesis we need to comprehend what and how erosion occurs as well as to make sense of all the mathematical models that were used.

2.1 Erosion

Erosion is the action of surface processes that removes soil or surface material. There are different types of erosion. The erosion mechanism that was taken into account in this thesis was particles that impact a wall and mass from the wall is lost.

Erosion is when mass is eroded away from the material surface due to physical or chemical interaction. Any industrial process involving the transport of solid particles entrained in a fluid phase can be subjected to erosion damage. Erosion often occurs in pipe bends, tube constrictions, and other structures that alter the flow field, such as pipelines and valves in the oil and gas industry.

In the petroleum industry, it is important to make wells economically viable, flow rates must be high in order to justify the huge amounts of resources that must be utilized to find and produce oil and gas. Higher throughput is preferred because of the advantage of having higher production rates and lower liquid holdups. In the oil and gas industry, pipe structures and valves are exposed to high flow rates and pressures, which leads to material loss of the pipe wall or the valve. If the inner walls were to fail due to erosion, the consequences can be severe environmentally and economically. The production must stop for maintenance and the damaged part must be replaced, which is a costly operation. Sand production has the highest significance consequences for both production and assets. Sand production may even cause harm to people or the environment. Several key failures are related to erosion by sand. For most oil and gas fields, sand from reservoir formation is an inevitable by-product. That is why it is important to monitor and control the sand production. Having good erosion estimates are key to keep the production safe and economical.

To optimize the design of process equipment and the piping system, it is important to identify the location and magnitude of the maximum erosion rate for multiphase flows. Being able to simulate the erosion of a desired geometry, it is possible to produce better valve structures and choose optimal material and thickness. Optimal components will have a longer lifetime and less maintenance.

Production choke valves generally stand out as the components in oil and gas production systems that are most susceptible to erosion. This is primarily due to the potential high flow velocities

created by the pressure drop across choke valves. In addition to the risk associated with erosion, production choke valves are also susceptible to plugging in cases of high sand concentrations or particles larger than the passage through the throttling part of the choke valve [1].

There are several ways to measure the erosion wear, the most common is *erosion rate*. Erosion rate is defined as mass of wall removed per unit area per unit time. Some researches also use the expression erosion ratio, that is, the mass of wall material eroded per unit mass of impinging particles. This thesis uses erosion rate multiplied with the wall area to get the *overall erosion rate* in the mass of wall eroded per time unit.

2.1.1 Clean-up

After completion and perforation of a oil and/or a gas well, the borehole is filled with completion and perforation fluids. During perforation some metal and fines come off. When the choke valve opens for the first time a lot of debris will start flowing through, such as metals and fines. First the completion fluid will come up, followed by nitrogen if it is needed to lower the pressure in the borehole to get a better clean-up. The reservoir fluids that push the completion fluids out come right after with a smaller amount of debris. The formation fluids will be sent to the rig or platform for processing [2]. However, even under normal production some fines together with sand may come up even after the clean-up operation, which is the main cause of erosion damage and we focused on in this study.

2.2 Computational fluid dynamics (CFD)

CFD is a tool to simulate fluid flow systems by using modeling and numerical methods. First a geometry is required defined by mathematical and physical formulation inside the CFD program. After modeling the geometry there are several *numerical methods*, which can be applied to the geometry such as discretization methods, solvers, process parameters, grid generation, etc. Being able to use numerical simulations instead of physical experiments is beneficial both economically and time-wise. Instead of using a lot of effort on a physical experiment, it is possible to carry out *CFD experiments* anywhere [3]. This makes the numerical experiments valuable in situations where physical experiments are difficult to be carried out in practice. The CFD software used in this thesis was the STAR-CCM+ version 13.06.012-R8 from Siemens. This tool provides the user the ability to model complex geometries, then apply the numerical methods and make use of models for taking into account different physical phenomena. Simulations can be performed by running on cores in parallel, and post-processing tools are available in the program.

2.2.1 The governing equations of CFD

The physical aspects of any fluid flow are governed by three fundamental principles of the continuity, momentum and the energy [3]:

1. Mass is conserved
2. Newton's second law (Force = Mass x Acceleration)
3. Energy is conserved

To investigate a fluid flow, we have to know the physical properties of the flow and use mathematical formulations to describe the physical properties. An important point is to *derive* the governing

equations. These equations can be obtained in various forms: integral or partial differential equations in conservation or non-conservation form. For a given algorithm in CFD, the use of the equations may lead to converging results while others diverge, leading to instability or oscillations. The partial differential equations are derived from an infinitesimally small volume, while the integral equations are derived from a finite control volume. In both cases, the fluid element can be either fixed in space or moving with the flow. This results in *four models of flow*. The element fixed in space will give equations in the conservation form, while the element moving with the flow results in the non-conservation form of these equations.

Viscous flows are described by the fundamental flow equations called the Navier-Stokes equations. If a flow is viscous, transport phenomena of friction, thermal conduction and/or mass diffusion are included. These effects will always increase the entropy of the flow. On the other hand, we have inviscid flow where the equations are called Euler equations. Inviscid flow is, by definition, a flow where the dissipative, transport phenomena of viscosity, mass diffusion, and thermal conductivity are neglected.

Continuity equation

The governing flow equation, which results from the application of the physical principle *Mass is conserved* to any of the four models of flow described above. The equation is called the *continuity equation*, which states that:

Rate of mass accumulated inside fluid the element

=

Rate of mass flow into the element - Rate of mass flow out of the element

As the geometry is fixed in space, the conservation form of the equation is used in this thesis [3].

Momentum equation

The governing flow equation, which results from the application of the physical principle of Newton's second law is the momentum equation. When applying Newton's second law to a moving fluid element, it tells us that the net force on the fluid element equals its mass times the acceleration of the element. There are two different sources of forces acting on the moving fluid element [4].

1. *Body forces*: these forces act directly on the volumetric mass of the fluid element at a distance from it. Examples are gravitation, electric, and magnetic forces.
2. *Surface forces*: these forces act directly on the surface of the fluid element. The outside fluid imposes two sources of surface force, pressure, and viscous forces. The pressure force involves the total pressure acting on the element surface by the surrounding fluid. The viscous forces include the shear, and normal stress distribution acting on the surface, imposed by the outside fluid by means of friction.

Again the conservation form of the equation is used in this thesis.

Energy equation

The energy equation is based on the physical principle of energy conservation, which also is the first law of thermodynamics. The physical principle states that the total energy of an isolated system is constant. Energy can be transformed from one form to another, but can not be created or destroyed. When applying this principle to any of the fluid flow models [3], it states that:

Rate of change of energy inside fluid element

=

Net flux of heat into element

+

Rate of work done on element due to body and surface forces

The energy equation was not used in this thesis.

2.2.2 Discretization and mesh

According to Anderson [3], discretization is the process by which a closed-form mathematical expression, described in section 2.2.1, is approximated by analogous expressions that prescribe values at only a finite number of discrete points in the domain. This makes it more suitable for numerical computations. The closed form expression gives the variation of the dependent variable continuously through the domain, while the numerical solution only give answers at discrete point in the domain, called grid points.

Discretization in a CFD simulation is to divide the continuous domain into a finite number of discrete sub-domains, here cells. The next step is to store the unknowns at specific locations of the mesh, like vertices, grid points, or edges. Finally, the equations are used for discretization in time and space. The result is a coupled system of algebraic equations that need to be solved at each time-step [5]. The sub-domain is dependent on how the mesh is generated, by size and shape. Different number of cells and the form of the mesh will determine the accuracy of the numerical solution obtained.

The two CFD techniques for solving the resulting algebraic equations are the explicit approach and the implicit approach. In the explicit approach, each equation contains one unknown and can therefore be solved in a straightforward manner. On the other hand, the implicit approach has several unknowns. As a result, we only receive an answer by solving the equations simultaneously. By using the implicit approach the stability is maintained over a larger time-step, Δt, in contrast to the explicit approach. This is an important advantage as well as the computational time decreases.

2.2.3 Physical boundary and initial condition

When we look at different flows of fluid, the governing equations are the same. The only thing that can separate the flow solutions from each other is the boundary conditions. The boundary conditions describe the direction of the flow and dictate the particular solution from the governing equations. It is important to apply certain physical boundary conditions on the particular geometry surface for the numerical solutions to be accurate.

Walls constitute the most common boundary in confined fluid flow problems. The walls are normally impermeable and stationary, or moving with the flow. The boundary condition for viscous flow on a surface assumes no relative velocity between the wall surface and the fluid in immediate contact with the surface. This is called a *no-slip* condition. There are also boundary conditions that allows the fluid to enter and exit the computational domain, called *inlet boundary* and *outlet boundary*, respectively. If the flow field is symmetric, it would be beneficial to use symmetric boundary conditions. This would reduce the computational domain and thus save memory and time. In this thesis, a unique geometry was studied and the boundary symmetry could not be used.

The *initial conditions* describe the values of the flow field variables at $t = 0$. It is most common to set the pressure, temperature, velocity quantities and velocity components, but for more complex

simulations other physical parameters can also be set. For a steady-state problem the converged solution should be independent of the initial field. However, it affects the path to convergence. Therefore, it is important to choose the initial conditions and values judiciously when the physics is complex.

2.3 modeling multiphase systems

Multiphase systems are systems consisting of a continuous phase and one or more dispersed phases mixed at a macroscopic level, where a two-phase system is the simplest case. Each phase is defined by the thermodynamic states gas, liquid or solid. The flow characteristics follows a dispersed phase flow, and thus the governing flow equations need to be modified. Therefore, we need to introduce a phase coupling.

2.3.1 Phase coupling

When there is more than one phase in a system, the phases can affect each other. The simplest one is *one-way coupling*, where the continuous phase affects the dispersed phase but not the other way around. If the dispersed phase also affects the continuous phase it is called *two-way coupling*. In general, the dispersed phase is driven by the motion of the continuous phase. The interaction strength between the two phases depends on parameters like size, density, and number of dispersed phase particles.

2.3.2 CFD-based erosion modeling

There are many factors that influence the erosion process such as material properties, particle size, geometry, flow velocity, pressure, turbulence, and multiphase flow interactions. These factors interact with each other, which is why accurate inputs are important for best possible results. CFD is a powerful tool that can be used to study the effect of different parameters of erosion rate, predict the maximum erosion rate, even in complex geometries in which setting up an experimental study is difficult or simply too expensive. Many researchers have developed different erosion models, which are later discussed in Chapter 3.

To describe erosion by using CFD analysis, there are three main steps that will be used in this thesis: flow modeling, particle tracking, and relating particle-wall impact information to model erosion damage. Each step is dependent on the previous one. Therefore, any non-physical result in any of the three steps affect the final result. Fig. 2.1 summarizes the three steps of the CFD-based erosion simulation.

2.3.3 Turbulence

It has been known for a long time that fluid can flow through a pipe in two different ways. The distinction between the two flow types was first demonstrated in an experiment by Reynolds, reported in 1883 [6]. Reynolds found out that when the colored water flowed parallel with the flow, the flow was laminar. This occurred at low fluid flow rates. When the flow rate was increased, a *critical velocity* was reached where the thread of color became wavy and gradually disappeared. As the flow no longer was laminar and moved erratically in the form of cross-current and eddies it

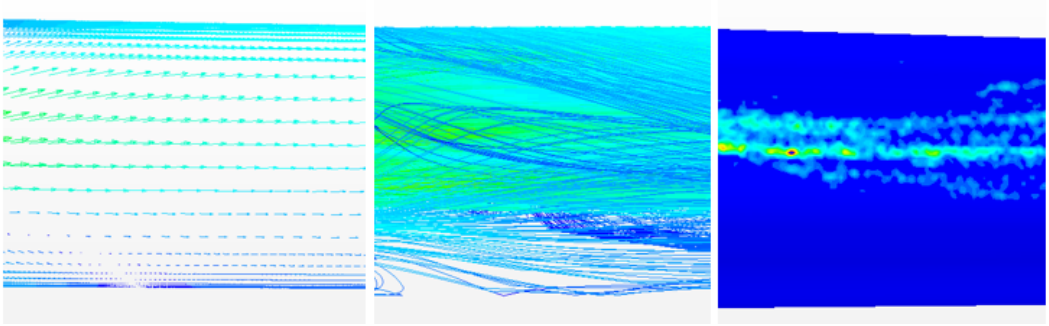

Figure 2.1: The three steps to CFD-based erosion modeling illustrated: flow modeling, particle tracking, and erosion modeling.

became *turbulent*. Reynolds suggested a dimensionless number, which describes this phenomenon:

$$Re = \frac{D\bar{V}_f \rho_f}{\mu_f}, \tag{2.1}$$

where D is the diameter of the tube, $\bar{V}_f$ is average the velocity of the fluid, μ_f is the viscosity of fluid, ρ_f is the density of the fluid, and Re is the Reynolds number. From the experiments, they found that under ordinary conditions, the flow in a pipe or tube is turbulent at Reynolds numbers above 4000 [4].

Solving turbulent flow can be done directly by using the Navier Stokes equations. This is very computationally expensive and takes a long time to simulate because of the small scale and high frequency of fluctuations. Thus, instead of using Navier Stokes, STAR-CCM+ uses Reynolds-Averaged Navier Stokes (RANS) equations. Here the equation estimates the impact of the small scale fluctuating structures. The most common RANS turbulence model in STAR-CCM+ is the two equation $k-\epsilon$ model, which solves the transport equations for the turbulent kinetic energy and its dissipation rate to determine the turbulent viscosity. This is necessary to model the turbulent stress tensor, τ^t, which appears in the momentum transport equation in the averaging process. Alternatively, there exist $k-\omega$ and RSM turbulence models. Each of these models has advantages and disadvantages. They provide flow field predictions at various conditions and geometries with different accuracy. To choose a suitable turbulence model it is required to understand the flow characteristics in the system of interest. Nevertheless, choosing a turbulence model is not the only preparation for CFD modeling, the mesh also needs to be well suited for the geometry. Considering that the results from flow modeling are used to predict erosion, it is essential to accurately model the flow field [7].

2.3.4 Continuous phase

The first step in erosion damage prediction is to model the flow, here the continuous phase. The continuous phase, which also is a carrier fluid, can be either in liquid or gas form. For this thesis the continuous phase will be gas and the dispersed phase is sand. The carrier gas flow can be simulated by different laws in STAR-CCM+. The three models in STAR-CCM+ are:

Ideal gas law is a combination of several gas laws. It describes the behavior of an *ideal* gas. It assumes negligible molecular interaction, and negligible volume occupied by the molecules themselves. To relate properties at one condition to another, we use the PVT relationship provided by

an *equation of state*. The simplest equation of state is the ideal gas law:

$$PV = NRT,$$

where P is the pressure of the gas in [Pa], V is the volume in [m^3], T is the temperature [K], N is the amount of gas [mole] and R is the universal gas constant 8.314 [Joules $mole^{-1}K^{-1}$], [8].

Real gas models are used in simulations where the gas properties cannot be explained using ideal gas law, for example, near condensation point of gases, near critical points and at high pressures [5]. In this thesis Van der Waals real gas model was used due to the high pressure and temperature on the choke, the equation is given by:

$$(P + a/V^2)(V - b) = RT \tag{2.2}$$

where Van der Waals replaced specific volume in the ideal gas relation, $PV = NRT$, with $(V - b)$ to account for the volume that the particles of the gas occupy, while replacing the pressure with the term $(P + a/V^2)$. The constant b is the co-volume of the particles, and a is a measure of the attractive forces.

Incompressible fluids are fluids whose density and related properties are relatively insensitive to pressure. As most liquids are incompressible, most gasses are compressible. Therefore, their properties are typically functions of T and P.

2.3.5 Lagrangian vs. Eulerian multiphase

The second step to find the erosion rate using CFD is determining particle motion of the dispersed phase. STAR-CCM+ has two main particle-modeling approaches when simulating multiphase systems. The first one is the Lagrangian and the second one is the Eulerian method. In the Lagrangian multiphase the continuous phase can be treated in different ways, as segregated, coupled or an Eulerian continuous flow. Segregated flow does not account for the presence of the dispersed phase, that is, one-way coupling. The coupled and Eulerian flow do take the presence of the dispersed phase into account. On the other hand, the Eulerian multiphase model can only be used while also having the Eulerian flow model as well, therefore it is called the Eulerian-Eulerian approach (E-E).

The main difference between these two approaches is how they consider the dispersed phase. The dispersed phase can be treated either in the Lagrangian or the Eulerian frame of reference in numerical simulations. The first model, Lagrangian, track particles individually as they move through the continuous phase, and then solves the equation of motion for each particle, which includes forces acting on the particle. This method also assumes that the particle is smaller than the mesh cells and gives very accurate particle motion. The disadvantage is that the approach is computationally expensive for a large number of particles. In contrast, we have the E-E model, which considers the dispersed phase to be a continuous phase. Then the Navier Stokes equations are solved for each phase present.

The following equation shows the particle equation of motion commonly used in CFD [9]:

$$\frac{d\bar{V}_p}{dt} = F_D + F_V + F_P + F_G. \tag{2.3}$$

In Eq. (2.3), the right-hand side represents the forces acting on the particle, and the left hand side is the particle inertia. Drag force, F_D, is the most important force acting per unit particle mass:

$$F_D = \frac{18\mu_f C_D Re_p}{\rho_p d_p^2 24} \left(\bar{V}_f - \bar{V}_p\right). \tag{2.4}$$

Virtual mass is another force that affects particle trajectories. Virtual mass is a force that represents the volume of fluid which is displaced by an accelerating or decelerating particle. When the density ratio between the dispersed and continuous phase is large, this force cannot be neglected. This force can be written as:

$$F_V = \frac{1}{2}\frac{\rho_f}{\rho_p}\frac{d}{dt}\left(\bar{V}_f - \bar{V}_p\right). \tag{2.5}$$

When a particle passes through areas with a high-pressure gradient, the force due to the pressure gradient can impact the particle trajectory. The following equation describes the pressure gradient force:

$$F_P = \left(\frac{\rho_f}{\rho_p}\right)\bar{V}_{p_i}\frac{d\bar{V}_f}{dx_i}. \tag{2.6}$$

Other forces which can affect the particle trajectories are gravity and buoyancy:

$$F_G = \frac{(\rho_p - \rho_f)\, g}{\rho_p}. \tag{2.7}$$

Saffman lift force can be included in Eq. (2.3). It is a force resulting from shear in the flow. Particle trajectories can be found by solving Eq. (2.3).

From the Lagrangian model, we have two approaches for numerical simulation of particles: the *discrete element method* (DEM) and the *discrete parcel method* (DPM). In STAR-CCM+ it is only possible to choose the DEM method for unsteady simulations, while for steady-state simulations the DPM method is used by default. For the E-E model, there is one approach for numerical simulation of particles: *two-fluid model*. These three methods are illustrated in Fig. 2.2.

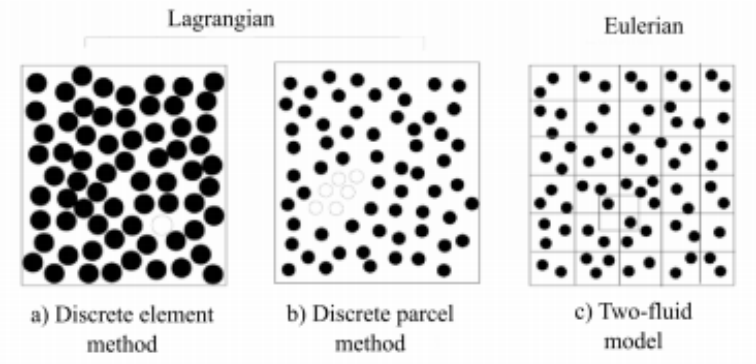

Figure 2.2: Three main approaches for numerical simulation of particles, illustration from [10]. a)DEM; b) DPM and c) E-E.

In DEM, the motion of each particle is analyzed incorporating the fluid dynamics forces, the contact forces and the momentum due to the neighboring particles. An alternative Lagrangian approach that requires less computational time is the DPM, where parcels of particles are identified when moving through the field. The third approach is the E-E model. This model considers the dispersed solid phase as a continuous phase like the carrier fluid. This method is less computationally expensive than the Lagrangian approach when we look at many particles. However, using the E-E method can pose a problem in the prediction of particle behavior close to a wall. In this region, particle motion consists of impacting and rebounding, where the E-E method only gives a mean value of particle motions in each control volume. This can cause inaccurate particle impact velocity,

which again influences the erosion prediction [11]. The behavior and how each particle interacts with each other has a significant impact on the erosion of the choke. For this reason, the most accurate and suitable modeling approach for the dispersed phase in this thesis is the Lagrangian DPM approach.

2.3.6 Particle collision and interaction

When a particle impacts a wall, it loses some of its kinetic energy. A restitution coefficient is used to account for this energy loss. It is defined as the ratio of the final velocity to the initial velocity between two objects after their collision. The restitution coefficients e_n and e_t illustrate the change in particle momentum through the collision in the normal and tangential direction to the wall, respectively:

$$e_n = \frac{\bar{V}_{pn2}}{\bar{V}_{pn1}} \tag{2.8a}$$

$$e_t = \frac{\bar{V}_{pt2}}{\bar{V}_{pt1}} \tag{2.8b}$$

$\bar{V}_{pn}$ and $\bar{V}_{pt}$ are the particle velocity normal and tangential components, respectively. Subscript 1 describes the case prior to the collision and subscript 2 refers to the case after the collision. If the coefficient of restitution is 1, it indicates that there is no momentum loss during the impact: this case is called elastic rebound. The coefficient of restitution of 0 means that the particle loses all its momentum during the impact. Physically this means that the particle sticks to the wall after impact.

Erosion occurs when particles hit walls. When particles impact the wall, the impact information such as impact speed and impact angle of each particle in each CFD computational cell next to the wall are saved. The third step in predicting the erosion is to feed the impact information into an erosion equation. Information from each impact is used in an erosion equation to calculate surface mass loss that each particle causes. The overall erosion rate is the summation of all mass losses that all particles cause.

2.3.7 Wall treatment

Walls are a source of vorticity in most flow problems of practical importance. Therefore, an accurate prediction of flow and turbulence parameters across the wall boundary layer is essential. The non-dimensional wall distance y^+ is given as:

$$y^+ = \frac{yu*}{v} \tag{2.9}$$

where

$$u^* = \sqrt{\frac{\tau_w}{\rho}} \tag{2.10}$$

In these equations y is the normal distance from the wall to the wall-cell centroid, v is the kinematic viscosity, u^* is a reference velocity, τ_w is the wall shear stress and ρ is the density.

The inner region of the boundary layer can be split into three sublayers. In each of them the flow has different characteristics and can be modeled using different empirical approaches [5]:

Viscous sublayer is when the fluid layer in contact with the wall is dominated by viscous effects and is almost laminar. The mean flow velocity only depends on the fluid density, viscosity, distance from the wall, and the wall shear stress. Usually for the non-dimensional wall distance $y^+ \leq 5$.

Buffer layer is when the buffer layer is a transitional layer between the viscous sublayer and the log-law layer. The wall distance is in the range of $5 < y^+ \leq 30$.

Log-law layer is when the turbulent log-law layer is dominated equally by viscous and turbulent effects. Wall distance is in the range of $30 < y^+ \leq 500$.

STAR-CCM+ provides three different wall treatments. This thesis will only use the *all-y*$^+$ wall treatments for RANS called *two-layer all-y*$^+$. This is a hybrid treatment and emulates the *low-y*$^+$ wall treatment for fine meshes, and *high-y*$^+$ wall treatment for coarse meshes. Low-y^+ wall treatment resolves the viscous sublayer and needs little to no modeling to predict the flow across the wall boundary. The transport equations are solved all the way to the wall cell. The wall shear stress is computed as in laminar flows. The high-y^+ wall treatment does not resolve the viscous sublayer. Instead wall functions are used to obtain the boundary conditions for the continuum equations. Wall shear stress, turbulent production, and turbulent dissipation are derived from equilibrium turbulent boundary layer theory. The all-y^+ is also formulated with the desirable characteristic of producing reasonable answers for meshes of intermediate resolution, that is, when the wall-cell centroid falls within the buffer region of the boundary layer. A blending function is then used to calculate turbulence quantities such as dissipation, production, and stress tensor.

The two-layer all-y^+ wall treatment uses an approach identical to the all-y^+ wall treatment, but contains a wall boundary condition for ε that is consistent with the two-layer formulation of the $k - \varepsilon$ and Reynolds Stress turbulence models.

2.3.8 Residuals

The residuals in each cell represent the degree to which the discretized equation is satisfied. They are created automatically within every simulation. However, it is important to understand both the significance of residuals and their limitations. While it is true that the residuals tend toward a small number when the simulation is converged, the residual monitors cannot be relied on as the only measure of convergence. When a solver is run, a discretized version of the equations selected is solved for each cell in the mesh. Residual monitors in STAR-CCM+ keep a record of the global quantity *root mean square* (RMS) for each of the transport equations solved inside the fluid flow volume. This value is automatically normalized to values from 0 through 1. In general, residuals are used to monitor the behavior of the solvers at each iteration to make sure that the solution converges towards the machine precision.

2.3.9 Courant-Friedrichs-Lewy condition

When operating with finer meshes the Courant-Friedrichs-Lewy condition (CFL) is a necessary condition for convergence. The principle behind the condition is that, if we want to compute anything across a discrete grid at discrete time steps of equal duration, then this duration must be less than the time for the simulated fluid or particle to travel to an adjacent grid point. As a corollary, when the grid point separation is reduced, the upper limit for the time step also decreases. In principle, the numerical domain of dependence of any point in space and time must include the analytical domain of dependence to assure that the scheme can access the information required to form the solution [12].

CFL for steady-state simulations increases the local pseudo-time step size and produces faster convergence for the residuals. Thus, it is important to use the largest possible CFL number while still ensuring that the solver remains within the bounds of stability. For finer meshes, it is better to start the simulation at smaller CFL numbers and increase it gradually, while ensuring a stable decrease in the residuals [5]. An indication of convergence is when the residuals reach a desired low value and when the fluid properties stabilize, such as velocity and pressure loss.

2.4 Pressure loss

There will be pressure loss, ΔP, over both straight pipelines, and complex geometries on pipes. The pressure drop comes due to friction, obstacles and geometry. By using the Bernoulli equation with friction we can find the pressure drop:

$$\frac{\alpha_a \bar{V}_{fa}^2}{2} + \frac{P_a}{\rho} = \frac{\alpha_b \bar{V}_{fb}^2}{2} + \frac{P_b}{\rho} + h_f. \tag{2.11}$$

The term h_f represents all the friction generated per unit mass of fluid that occurs in the fluid between stations a and b. In potential flow, the h_f term is zero, for any other flow it is always positive. Assuming the fluid is incompressible the kinetic energy correction factors, α_a and α_b, and the velocities, $\bar{V}_{fa}$ and $\bar{V}_{fb}$, are assumed to be the same, which let us rewrite the Eq. (2.11) to:

$$P_a - P_b = \Delta P = \rho h_f. \tag{2.12}$$

In the simplified Eq. (2.12) we can see that the pressure loss is linearly dependent on the density of the fluid, which again is dependent on temperature and pressure [4]. From this term, we can already see that for higher pressures the pressure drop will be higher.

2.4.1 Friction

Friction comes from changes in the velocity, in either direction or magnitude. It is generated in addition to the skin friction resulting from flow through a straight pipe. This includes form friction resulting from vortices when normal streamlines are disturbed. Sudden expansion or sudden contraction of a pipe are examples of disturbances of the streamline.

Friction loss in a straight tube is dependant on the velocity, friction factor, diameter and length of the tube. The *friction factor*, f, can be found by using a friction factor chart by Moody [13]. A sketch of the geometry is presented in Fig. 2.3. The equation is:

$$h_{f_s} = 4f \frac{L}{D} \frac{\bar{V}^2}{2}. \tag{2.13}$$

Sudden expansion of a pipe is when the diameter of the pipeline suddenly increases, the fluid stream will then separate from the wall and issues as a jet into the larger section. The jet will expand to fill the entire cross-section. The space where the jet does not touch any walls is filled with fluid in vortex motion and boundary layer separation. In this region considerable friction is generated, see Fig. 2.4a.

The friction loss due to the sudden expansion of cross-section, h_{f_e}, is proportional to the velocity in the small conduit and can be written:

$$h_{f_e} = K_e \frac{\bar{V}_{fa}^2}{2}, \tag{2.14}$$

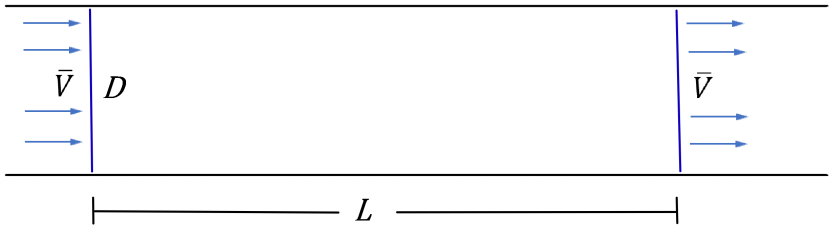

Figure 2.3: Straight tube.

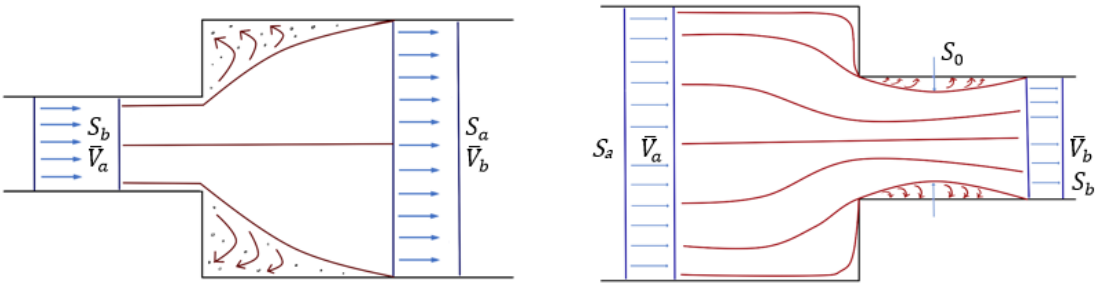

(a) (b)

Figure 2.4: (a) Sudden expansion and (b) sudden contraction

where $\bar{V}_{fa}$ is the average velocity in the smaller, upstream, conduit and K_e is the *expansion loss coefficient*. The expansion loss coefficient utilizes the continuity equation, the steady-flow momentum-balance equation, and the Bernoulli equation so that:

$$K_e = \left(1 - \frac{S_b}{S_a}\right)^2, \tag{2.15}$$

where S_a is the surface area of the larger conduit and S_b is the surface area of the smaller conduit [4].

Sudden contraction occurs when the cross-section of the conduit suddenly reduces. The flow at the edges breaks the contact with the wall due to the sharp corner. As such, a jet is formed through the smaller conduit. At first, the jet contracts and then expands to fill the smaller cross-section downstream. The minimum cross-section area where the jet goes from contraction to expansion is called *vena contracta*, S_0, where we find the highest velocity. This is illustrated in Fig. 2.4b.

The friction loss due to the sudden contraction, h_{f_c}, is proportional to the velocity in the smaller conduit and can be written as:

$$h_{f_c} = K_c \frac{\bar{V}_{fb}^2}{2}, \tag{2.16}$$

where $\bar{V}_{fb}$ is the average velocity in the smaller, downstream, section and K_c is the *contraction loss coefficient*. For turbulent flow K_e is given by the empirical equation:

$$K_c = 0.4\left(1 - \frac{S_b}{S_a}\right), \tag{2.17}$$

where S_a and S_b are the cross-section areas of the upstream and downstream conduit, respectively [4].

Effect of fittings and valves, these types of hindrances disturb the normal flow lines and cause friction. The friction loss from fitting, h_{f_f}, from an equation quite similar to Eq. (2.14) and Eq. (2.17):

$$h_{f_f} = K_f \frac{\bar{V}_{fa}^2}{2}, \tag{2.18}$$

where K_f is the loss factor for a fitting and $\bar{V}_{fa}$ is the average velocity in the pipe leading to fitting [4].

The K_f factor is found by experiment and differs for each geometry connection. Elbows of 90° have K_f of 0.75 [14].

Chapter 3

Literature survey

Researchers have performed several studies on erosion models to understand its mechanisms and to choose the right type of material when developing new pipeline systems. This section provides an overview of some relevant erosion experiments performed on 90° elbows and chokes, as well as CFD based erosion modeling.

3.1 Particle properties

Particle properties such as size, density, hardness, and shape have a significant influence on solid particle erosion. Several researchers have looked at the effect of each particle property on erosion.

3.1.1 Particle shape

Salik et al. [15] showed that the particle shape could change the erosion rate by an order of magnitude. Levy and Chik [16] observed the same behavior and reported that the shape of particles has a huge influence on the magnitude of erosion. They used two different particle shapes, sharp angular and spherical particles. Angular particles gave four times larger erosion compared to spherical particles. It also had been reported that the impact angle with maximum erosion depended on particle shape and varies based on particle angularity by Huchings et al. [17]. Arabnejad et al [18] did several experiments where one of the experiments at the Erosion/Corrosion Research Center (E/CRC) showed that well-rounded particles cause four to five times less erosion than very angular particles. As a result, it is considered that small sharp particles *can* be more erosive than large semi-rounded particles [9].

3.1.2 Particle size

Particle size is another important particle property. Larger particles have larger kinetic energy even if they strike a target with the same velocity. Tilly [19] reported erosion data as a function of particle size. His result indicates that erosion ratio is nearly independent of particle size when the particles are larger than approximately 100 μm. Gandhi and Borse [20] investigated the effect of sand size on cast iron erosion behavior for two different impact angles: 30° and 75°. The velocity was 3.62 m/s and sand concentration 20 wt%. They observed a linear relationship between sand

size and erosion rate. This behavior was also reported by Elkholy [21] and Clark [22]. These results are influenced by the fact that the particle impact velocity is not constant and changes with particle size when particles are entrained in liquid streams.

Desale et al. [23] examined the effect of particle size on erosion performance of an aluminum alloy for eight different sizes of silica sand. They concluded that at a constant sand concentration, increasing the particle size increases the erosion rate even though it reduces the number of particles. Particle impact velocity and kinetic energy per impact are affected by particle size. Desale et al. suggested a correlation between erosion rate and particle size:

$$Erosion\,rate \propto (Particle\,size)^n. \tag{3.1}$$

The n value is between 0.3 and 2.0 depending on the differences in material properties, experimental conditions, particle velocity, particle size, and size distribution. They said that in most cases, n is one, and a linear relation is observed between sand size and erosion rate. Oka et al. [24] and Oka and Yoshida [25] introduce a particle size factor in their erosion ratio model, which was raised to the 0.19 power.

In general, smaller sand particles cause lower erosion rates because they have smaller kinetic energy and impact force to erode the surface. For sand particles of the same impact speed, shape, density, and hardness, larger particles will cause more erosion damage. However, the smaller particles are easier affected by the surroundings. Turbulence is one of these factors, the exchange of momentum between fluid and particle is more efficient for smaller particles, so they respond to fluctuations in the flow more easily. Particle-particle iterations also affect small particles more than larger particles.

3.1.3 Particle material

Levy and Chik [16] also studied the effect of particle composition on erosion behavior of AISA 1020 CS. They used five different brittle particles with an angular shape to erode the steel at two different flow angles of 30° and 90° and a flow velocity of 80 m/s. Erosion ratio was low when soft erodents such as calcite and apatite were used to erode the steel. The hardest of the two, apatite caused slightly more erosion. However, when Vickers hardness of particles reaches values about 700 H_V, further increasing in the hardness of erodent particles does not considerably increase the erosion rate. It has been observed that there is a correlation between the hardness of the target wall, particle hardness, and erosion damage. The hardness of a material is measured by observing the ability the material has to resist deformation from a source. Soft particles may shatter when they collide with a wall. The smaller particles then have lower mass and kinetic energy, which leads to less erosion. Scanning electron microscopy (SEM) analyses of steel surface after an erosion attack also showed that breakup and adherence of soft particles to surface reduces the kinetic energy. Furthermore, it also covers the target surface with a layer of fragment particles, which reduces the erosion damage [16]. This means harder particles can be more erosive because they do not shatter as when they collide with a wall. Wada and Watanabe [26] proposed the following correlation to explain the relationship between erosion rate and the ratio of target to particle hardness:

$$Erosion\,Rate \propto (\frac{H_t}{H_p})^n, \tag{3.2}$$

where H_t is the target material hardness and H_p is erodent particle hardness, and n is an empirical constant. Later, Shipway and Hutchings [27] also examined the effect of particle and target wall materials on erosion behavior. They concluded from their experiments that increasing the ratio of erodent target hardness toward unity rapidly increases the erosion rate and reduces the velocity exponent of erosion rate.

3.1.4 Fluid properties

Many researchers studied the effect of fluid properties on particle behavior. Examples are works by Hinze [28] and Humphrey [29]. The continuous phase in any multiphase system will have a large influence on the erosion. The carrier fluid will determine the impact speed of particles on the wall. The characteristics of the continuous phase such as viscosity and density affect particle behavior and thus, affects the erosion pattern and magnitude. How much the carrier fluid affects the particles depends on the geometry and flow pattern. If a flow impacts a wall normally, the particles will also collide with the wall in the same direction and result in a higher erosion than a flow in a straight pipe where the flow is parallel to the walls. Fluid properties also affect the local particle concentration. This means that if the overall particle concentration is low, the local concentration can be high due to the flow pattern.

3.1.5 Target wall properties

Despite a lot of experimental data, the correlation between the target material and solid particles erosion rate is still unexplored. Finnie et al. [30] proposed that having target materials with higher hardness results in higher erosion resistance. However, Levy and Hickey [31] showed that material with higher hardness can result in higher erosion rate as compared to materials with lower hardness. Based on their observations, they proposed that ductility allows the surface to distribute particle impact kinetic energy by plastic deformation which can result in lower erosion rate. The toughness of the target material may be a better indicator for erosion, since increasing hardness may reduce the ductility and consequently increase erosion rate caused by the brittle mechanism. Foley and Levy [32] observed that if the local strength of the target material is less than a specific value, particles are able to remove the material with plastic deformation.

Arabnejad et al. [18] looked at the effect of erodent particle hardness on the erosion of stainless steel. A correlation was found between the normalized erosion ratio and particle hardness on a SS-316 target. It was observed that the hardness effect is significant when the hardness of the particle is less than the hardness of the target material. Furthermore, erosion ratio does not increase significantly when the particle hardness is relatively higher than the material hardness and the particle keeps its integrity during impact. When impacting particles are softer in comparison to the target material, they may deform during impact and their kinetic energy will not be effectively transferred to the target material.

3.1.6 Particle impact speed

Erosion rate has a direct relation with particle impact velocity:

$$Erosion\ Rate \propto (V_L)^n, \tag{3.3}$$

where V_L is the particle impact velocity and n is a constant. Different researchers have proposed different values for n. Smeltzer et al. [33] and Burnett et al. [34] observed that n can vary from 0.3 to 4.5. More recently, Oka et al. [24] and Oka and Yoshida [25] suggested that n is not a constant and depends on the hardness of the eroded material. They proposed a value ranging between 1.6 to 2.6.

3.1.7 Particle impact angle

Many researchers have observed that the erosion rate is also a function of impact angle. The effect of impact angle on erosion varies based on the surface material as previously mentioned. Erosion rate trends for ductile materials are different from brittle materials. For ductile materials, higher erosion rates occur at lower impact angles. This is due to more efficient formation and cutting of platelets by particles at lower angles. Because erosion for brittle materials results in cracking, maximum erosion occurs at near normal impact angles. Most materials used in the oil and gas industry have characteristics of both ductile and brittle materials. As a result, a variety of angle functions have been proposed, see the next paragraph.

3.1.8 Particle-wall interaction behavior

When simulating erosion in CFD we need a particle wall rebound model to calculate the dynamic particle movement, erosion rate, and the maximum erosion location. Several researchers have proposed empirical restitution coefficients models, for instance, Grant and Tabakoff [35] and Forder et al. [36]. In this thesis, these two models were used with different erosion prediction models to predict erosion wear. The Grant and Tabakoff rebound model was only used with the two erosion models that gave the best erosion predictions. The restitution coefficient in the normal direction, e_n, and in the tangential direction, e_t, represent the change in particle velocity after impacting the wall. The model developed by Forder et al. is given as:

$$e_n = 0.988 - 0.78\alpha + 0.19\alpha^2 - 0.024\alpha^3 + 0.027\alpha^4 \tag{3.4}$$

$$e_t = 1 - 0.78\alpha + 0.84\alpha^2 - 0.21\alpha^3 + 0.087\alpha^4 - 0.022\alpha^5. \tag{3.5}$$

The model developed by Grant and Tabakoff is given as:

$$e_n = 0.993 - 1.76\alpha + 1.56\alpha^2 - 0.49\alpha^3 \tag{3.6}$$

$$e_t = 0.988 - 1.66\alpha + 2.11\alpha^2 - 0.67\alpha^3, \tag{3.7}$$

where α is the impact angle.

3.1.9 Temperature effect

There are different hypotheses to explain the role of temperature on the erosion mechanism. Smeltzer et al. [33] observed erosion rate decreases by increasing temperature. Later, Levy [37] suggested that metal ductility increases by increasing temperature. Therefore, more particles kinetic energy is absorbed by plastic deformation, when particles collide with the wall. However, even after several experiments, the effect of temperature on erosion is still not certain.

3.1.10 Particle-particle interaction

In this thesis particle-particle (P-P) interactions are neglected. This is because the P-P interactions do have no influence on erosion magnitude other than in slurry erosion. An interesting effect called *shielding* is when we have high sand concentrations. When particles rebound from the wall, they hit particles that move towards the wall and slow them down. Therefore, depending on the fluid and geometry conditions, higher sand concentrations may result in a lower erosion rate. This was observed by both Brown et al. [38] and Deng et al. [39].

3.2 Erosion models

Over the years several researchers have suggested different erosion models, due to industrial importance. Most of these are empirical and later tested both in CFD analyses and in experiments. Star-CCM+ has five built-in erosion models; Ahlert, DNV, Neilson-Gilchrist, Oka, and Archard, which are some of the models that are described in this section. The Ahlert, DNV, Neilson-Gilchrist, and Oka correlations describe impact wear, from the direct impact of particles on the eroded surface.

3.2.1 DNV correlation

Det Norske Veritas (DNV) developed an erosion model for predicting the erosion of straight pipes, elbows, plugged tees, welded joints, and reducers. This model was developed based on numerous experimental data and numerical predicted results. The model is expressed as:

$$ER = AF(\alpha)\bar{V}_P^n \tag{3.8}$$

$$F(\alpha) = \sum_{i=1}^{8} (-1)^{i+1} A_i \alpha^i, \tag{3.9}$$

where ER is the erosion rate of the target and is defined as the wall mass loss per unit area and per unit time. $F(\alpha)$ is the impact angle function, A is a constant, with a default value of $2.9 \cdot 10^{-9}$ for steel, n is a constant exponent, with a default value of 2.6. The default coefficients for the DNV correlation are air-borne sand eroding CS, and are taken from Haugen [40]. The DNV correlation does not explicitly depend on particle diameter. However, the correlation was derived from experimental data observed for a mean particle diameter of 225 μm. The values of A_i are given in Table 3.1.

Table 3.1: Values of parameters in solid particle erosion

A_1	A_2	A_3	A_4	A_5	A_6	A_7	A_8
9.370	42.295	110.864	175.804	170.137	98.398	31.211	4.170

3.2.2 Model by Tabakoff

A semi-empirical model to predict erosion rate at different impact angles and velocities was developed by Tabakoff et al. [41]. They examined erosion by coal particles of different material surfaces. They assumed the erosion process can be characterized by two mechanisms at small and large impingement angles, α. It was pointed out that the produced model is applicable to small, intermediate and large impact angles as well as a combination of them. In their model, the effect of particle tangential restitution coefficient as a parameter that affects the erosion rate was taken into account:

$$ER = K_1 F(\alpha)\bar{V}_p^2(\cos^2\alpha)(1 - e_t^2) + f(\bar{V}_p, n) \tag{3.10a}$$

where:

$$e_t = 1 - 0.0016\bar{V}_p \sin\alpha \tag{3.10b}$$

$$F(\alpha) = \left\{1 + K_4 \left[K_2 \sin\left(\frac{\pi}{2}\frac{\alpha}{\alpha_m}\right)\right]\right\}^2 \tag{3.10c}$$

$$F(\bar{V}_p, n) = K_3 \left[\bar{V}_p \sin(\alpha)\right]^4 \tag{3.10d}$$

$$K_4 = \begin{cases} 1, & \alpha \leq 3\alpha_m \\ 0, & \alpha > 3\alpha_m \end{cases} \tag{3.10e}$$

In the above: K_1, K_2, and K_3 are empirical constants for specific surface material, see Table 3.2. α is the relative angle between the particle path and specimen surface, and α_m is the angle of maximum erosion.

Table 3.2: K values for stainless steel

K_1	K_2	K_3
$1.505101 \cdot 10^{-6}$	0.296077	$5.0 \cdot 10^{-12}$

3.2.3 Ahlert erosion model

An empirical correlation to predict the erosion rate for AISI1018 steel was developed by Ahlert [42]. The effect of erosion on dry and wet surfaces was also investigated, where he found that the erosion rate of a wet surface was about twice the erosion rate for the dry surface. According to his study, the erosion rate is given by:

$$ER = A(BH)^{-0.59} F_S \bar{V}_p^n F(\alpha), \tag{3.11}$$

where A is a material dependent constant, F_S is the shape factor, and n is a constant particle velocity exponent equal 1.73. The angle function $F(\alpha)$ is split into two ranges. For angles ranging from 0 to 15 degrees $F(\alpha)$ is a polynomial:

$$F(\alpha) = a\alpha^2 + b\alpha, \tag{3.12}$$

where a and b are constants. While for angles ranging from 15 to 90 degrees, $F(\alpha)$ follows a trigonometric relationship:

$$F(\alpha) = x\cos^2\alpha\sin(\alpha) + y\sin^2\alpha + z. \tag{3.13}$$

The constants x and y are constants in the impingement angle function $F(\alpha)$, whereas z is calculated internally. The default coefficients for the Ahlert correlation are for liquid-borne semi-rounded sand particles eroding aluminum, as given by McLaury [43] and others.

Table 3.3: Values for constants in impingement angle function for dry surfaces

x	y	z	a	b
$1.239 \cdot 10^{-9}$	$-1.192 \cdot 10^{-9}$	$2.167 \cdot 10^{-9}$	$-3.34 \cdot 10^{-8}$	$1.79 \cdot 10^{-8}$

3.2.4 Neilson-Gilchrist correlation

Neilson and Gilchrist [44] developed an erosion model based on their experimental results. They proposed two equations for predicting the erosion rate at small and large impact angles. The correlation is:

$$ER = ER_C + ER_D, \tag{3.14}$$

where ER_C and ER_D represent contributions from cutting and deformation respectively. The cutting erosion model as a function of the incidence angle α:

$$ER_C = \begin{cases} \frac{\bar{V}_P^2 \cos^2\alpha \sin\frac{\pi\alpha}{2\alpha_0}}{2\varepsilon_C} & \alpha < \alpha_0 \\ \frac{\bar{V}_P^2 \cos^2\alpha}{2\varepsilon_C} & \alpha \geq \alpha_0 \end{cases}, \tag{3.15}$$

where α_0 is the transition angle normally set to 45°, ε_C is the cutting coefficient, and $\bar{V}_P$ is the magnitude of the relative velocity of the particle with respect to the wall. The deformation erosion is similarly:

$$ER_D = \frac{max\left(\bar{V}_P \sin\alpha - K, 0\right)^2}{2\varepsilon_D} \tag{3.16}$$

with ε_D=7.742 $\cdot$ 10^7 is the deformation coefficient and K the cut-off velocity, below which no deformation erosion occurs. The default coefficients for Neilson-Gilchrist are for liquid-borne sand eroding AISI 4130 steel, and are taken from Wallace et al. [45].

3.2.5 Model by Haugen

A study of erosion in choke valves was performed by Haugen et al. [40]. They used a general correlation of erosion and empirically determined the coefficients of the equation:

$$ER = MK_pF(\alpha)\bar{V_p}^{n_p}, \tag{3.17}$$

where M is the mass of sand hitting the target material, $F(\alpha)$ is the same as for the DNV correlation, K_p and n are constants assumed to depend on the physical impact angle α. To obtain the coefficients 28 different material types were examined, and for each, they varied the impact angle and speed. Using the coefficients obtained for steel, a numerical simulation of the flow by using $k-\varepsilon$ turbulence model with Lagrangian particle tracking of sand particles was also performed. It was reported a good agreement between the proposed model and numerical simulation in the study with sufficient accuracy to be applied in the extrapolation of test results and for design purposes.

3.2.6 Oka et al. erosion model

Oka et al. [24] also proposed an empirical correlation similar to the E/CRC erosion equation. They modified the basic equation of dependence of erosion to impact velocity at the normal angle to take into account the effect of target material hardness, particle diameter, and particle properties:

$$E_{90} = K_p(H_V)^{k_1}(\bar{V}_p)^{k_2}\left(d_p \cdot 10^{-6}\right)^{k_3}, \tag{3.18a}$$

where $k_1$and k_3 are empirical exponent factors and k_2 is a function of the material hardness and particle properties. K_p is an independent factor denoting particle properties such as shape and hardness. They generalized the above equation for all impact angles by introducing an impact angle function as:

$$F(\alpha) = (\sin\alpha)^{n_1}(1 + H_V(1-\sin\alpha))^{n_2} \tag{3.18b}$$

$$ER = F(\alpha)E_{90}, \tag{3.18c}$$

where n_1 and n_2 are determined by material hardness or other impact conditions. Oka et al. identify the value of H_V as the Vickers hardness of eroded material in units of GPa. It was stated that the first term on the right-hand side of the impact angle function represents repeated plastic deformation and the second term represents cutting action. They achieved good agreement between the proposed model with aluminum, copper, carbon steel, and stainless steel erosion data.

In another study by Oka and Yoshida [25], other mechanical properties apart from hardness were used to find a correlation to predict erosion rate. Here they tested for work hardening and load relaxation ratio and proposed the erosion ratio:

$$ER = E_{90}F(\alpha)\left(\frac{\bar{V}_p}{v_{ref}}\right)^{k_2}\left(\frac{d_p}{d_{ref}}\right)^{k_3}, \tag{3.19a}$$

where the angle function is the same as Eq. (3.18b), v_{ref} is the user-specified reference velocity, d_{ref} is the user-specified reference diameter, and k_2 and k_3 are user-specified exponents. By inspection of Eq. (3.19a) and Eq. (3.18b), E_{90} is revealed to be the reference erosion ratio at $\bar{V}_p = v_{ref}$, $d_p = d_{ref}$ and $\alpha = 90°$. In STAR-CCM+ the value of E_{90} is calibrated by equating values for erosion ratio from the Oka and DNV models at 90° impact angle. The Oka reference particle size and velocity is $d_{ref} = 326\,\mu$m and $v_{ref} = 104$ m/s. This equation is:

$$E_{90} = ER_{DNV@90}\left(\frac{d_{ref}}{d_p}\right)^{k_3}. \tag{3.19b}$$

The purported strength of the Oka model is that the coefficients for a particular combination of eroded material, and eroding material can be derived from more fundamental coefficients. These coefficients are specific to either the eroded material or the eroding material. Hence, for example, the fundamental coefficients can serve as a basis for both sand-steel erosion and sand-aluminum erosion. The fundamental coefficients for the eroding material, in turn, are shown to be derivable from measurable properties of the eroding material such as its Vickers hardness. STAR-CCM+ bases the Oka correlation on the coefficients in Eq. (3.19a) and Eq. (3.18b). The default coefficients are for air-borne sand eroding 0.25% CS, taken from [24] and [25], except for E_{90} which is calibrated using the DNV correlation.

3.2.7 Archard erosion model

The Archard correlation [46] for erosion ratio is:

$$ER = aFs, \tag{3.20}$$

where a is the abrasive wear coefficient, with a default value of 0.01 kg/J. The default value of $1.0 \cdot 10^{-2}$ is the high end of the recommended range of values, $1.0 \cdot 10^{-8}$ to $1.0 \cdot 10^{-2}$, mild wear to severe wear, F is the normal force, and s is the sliding distance. The Archard correlation describes erosion due to scouring, where particles strike tangentially or at low angles. This model is one of the five built-in erosion models in STAR-CCM+. It is mostly used with DEM approach, which is why the Archard erosion model is not used in this thesis.

3.3 Erosion model comparisons

Several researchers have done experiments as well as simulation them using CFD. By comparing the CFD results to the experimental result, they can determine the best-suited model.

3.3.1 Vieira et al.

Vieira et al. [47] examined the erosion rate of a 90° elbow with a pipe diameter of 3 in. and 18 m long. The elbow was made of stainless 316 steel and had a curvature ratio r/D equal to 1.5. All the erosion experiments were performed in the vertically upwards inlet and horizontal outlet orientation (V-H) at near atmospheric pressure conditions.

First, they did the experiment and investigated four erosion models from literature. The predicted CFD erosion magnitudes using four empirical correlations proposed by Oka et al. [24], Zhang et al. [48], DNV [1], and Neilson and Gilchrist [44] were compared with present and previous Ultrasonic Testing (UT) erosion data in elbows. For all the comparisons, 100 000 particles were injected in the domain, and they used the coefficient of restitution model proposed by Grant and Tabakoff [35]. They also made their own erosion model namely Vieira et al. model in Fig. 3.1. Their erosion model is given by:

$$ER = 2.16 \cdot 10^{-8} F_S \bar{V}_P^{2.41} F(\alpha), \tag{3.21}$$

where

$$F(\alpha) = 0.65(\sin\alpha)^{0.15}(1 + 1.148(1 - \sin\alpha))^{0.85}. \tag{3.22}$$

Vieira et al. concluded that the erosion models tend to under-predict the erosion ratio. They noted that DNV and Neilson and Gilchrist correlations resulted in a lower erosion when compared to experimental results, whereas the other two correlations from literature displayed values closer to the experimental data. The correlations proposed by Oka et al. and Zhang et al. were the ones that showed a lower magnitude percent bias. However, both models also underpredicted experimental values. Fig. 3.1 shows an overall comparison between CFD prediction and the UT measurements. The horizontal axis shows the measured UT maximum erosion ratio in mm/kg in logarithmic scale, and the vertical axis shows the CFD predictions also in logarithmic scale.

3.3.2 Zhang and Liu

Zhang and Liu [49] examined four classic erosion models, E/CRC, DNV, Oka et al., and Grant and Tabakoff to calculate the penetration rates. By comparing the predicted results with the experimental data in literature, the comprehensive procedure was verified step by step. The experiments were performed by Bouroyne [50], Evans et al. [51], and Pyboyina [52]. All the experiments were of solid particle erosion in gas flow.

Fig. 3.2 shows the penetration rate (Pnr) defined as the thickness loss caused by per unit mass of solid particles, and the line denotes the points whose x-coordinate is equal to the y-coordinate. The best agreements would be closest to the diagonal line. The penetration rate is proportional to the erosion rate, $ER \propto Pnr$. They found good agreement over a broad range of penetration rates by applying the E/CRC, DNV, and Grant and Tabakoff equations. The erosion results predicted by Oka et al. equations were a little higher than the other predictions. The Grant and Tabakoff equations presented the best prediction among all the models. Zhang and Liu also calculated the brittle and ductile erosion separately and found that the expression exhibits more reasonable erosion predictions than the other models.

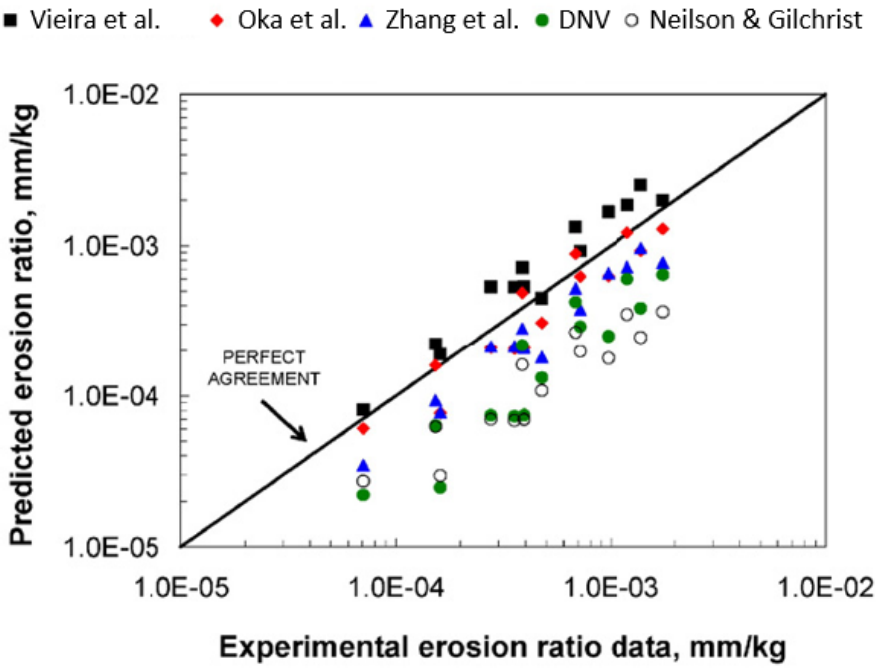

Figure 3.1: Comparison of present and previous UT data with CFD predictions for different erosion models [47].

3.3.3 Parsi et al.

Parsi et al. [53] employed six different erosion equations to discover which provided the best predictions. A good agreement was found between CFD results and the experimental data. Their main objective was to obtain erosion rates in a standard V-H elbow with r/D equal to 1.5 CFD-based, and compared it to the experiment by Parsi et al. [54].

In their study they assumed that the particle loading was sufficiently low so that the particle-particle interaction and effect of particles on the carrier phase were ignored, in other words, one-way coupling was assumed. Furthermore, Grant and Tabakoff particle-wall rebound model was used to account for particle-wall interactions for all the erosion models. This is essential in erosion calculations, as a particle may interact with a wall multiple times. They obtained mass removal curves from all 6 different erosion equations and plotted them. Clearly, different erosion models give different erosion rates. To compare the results with available experimental results, the CFD-based data were converted to erosion rates in mils per year. For all their examined cases, the Grant and Tabakoff, and DNV models delivered the highest and lowest erosion rates, respectively see Fig. 3.3. They found that the Mansouri erosion model gave the best prediction while Grant and Tabakoff erosion model overpredicted. The other erosion models underpredicted the erosion on the bend.

Parsi et al. [55] examined a 2-D CFD model to investigate erosion in standard elbows, r/D equal to 1.5, under different flow and particle conditions. Afterward, dimensional analysis was performed to first obtain the governing dimensionless groups and then extract self-similar behavior among them when plotted against the ratio of erosion rate divided by the gas velocity. This resulted in them defining the penetration rate $(ER/V_f) \propto (Pnr)^{1.0612}$ for their study. The penetration rate

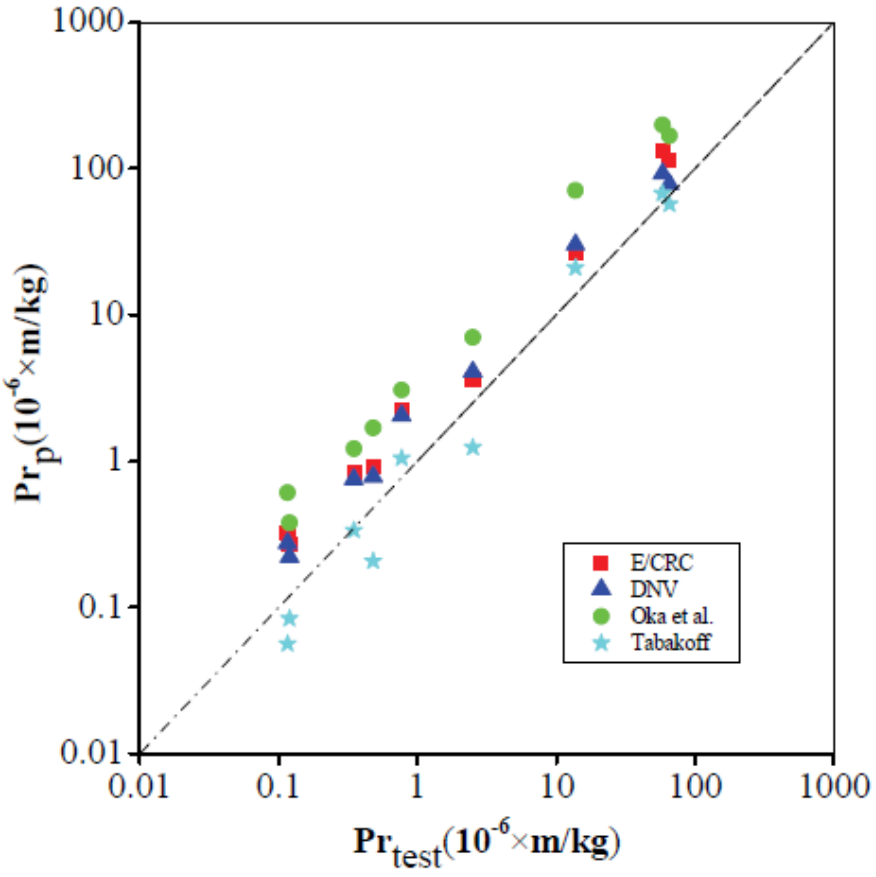

Figure 3.2: Comparison of penetration rates between erosion equations and experiments [49].

correlates the dimensionless erosion ratio to three dimensionless groups namely Reynolds number, diameter ratio, and density ratio that govern particle flow in elbows and hence erosion.

3.3.4 Peng et al.

Peng et al. [56] published a paper of erosion rate on a 90° elbow, with the same V-H orientation as in the work by Vieira et al. They stated that most of the erosion models for gas-solid flow had complex forms and only worked well within limits. In their work, a numerical erosion prediction model was developed for gas-solid flow with a simple form. They also compared several erosion models from literature. Fig. 3.4 shows the comparison between the predicted and the experimental erosion rate with different particle-wall rebound models. The results showed that the erosion rate calculated by the DNV erosion model and Forder et al. [36] particle-wall rebound model produces the most accurate results. Moreover, the results calculated by Grant and Tabakoff model provided lower values than those of the Forder et al. model.

In their subsequent paper [57], Peng et al. analyzed solid particle erosion in liquid flow, also in a 90° elbow. Here they looked at a two-way coupled E-L approach to solve a liquid-solid flow in a pipe bend in a grid with approximately 850 000 cells. An Eulerian simulation with $k-\varepsilon$ turbulence

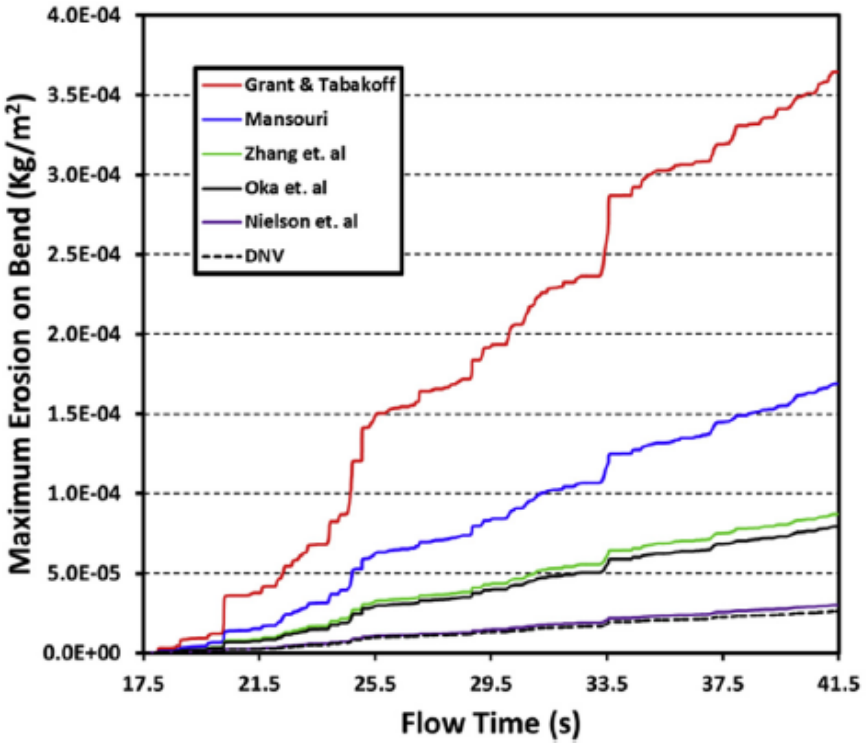

Figure 3.3: Maximum erosion on bend versus time: V_G=10.3 m/s, V_L=0.3 m/s, d_p=300 μm [53].

model was used to simulate the liquid flow in a pipe bend, while the Lagrangian particle tracking method was employed for calculating the particle motion. The liquid-solid interaction was also taken into account. They tested five different erosion models and to rebound models to predict the maximum erosion rate and location. They found that the E/CRC erosion model with the Grant and Tabakoff particle-wall rebound model gave the results closest to the experimental data from Bourgoyne [50].

Fig. 3.5 illustrates the penetration rate around the elbow obtained by five CFD-based erosion models and experimental by Zeng et al. [58]. We see that the Ahlert erosion model results in a higher penetration rate compared to the experimental data. The penetration rate by Oka et al. erosion model and Neilson and Gilchrist erosion model also overestimates the erosion rate. The prediction by DNV and E/CRC shows good agreement with the experimental data.

Fig. 3.6 shows the ratio of predicted penetration to experimental penetration lies in the range of 1.01-1.82 when the E/CRC and Grant and Tabakoff model are applied. It indicates that the prediction calculated by E/CRC with Grant and Tabakoff yields the best agreement with the experimental data.

Peng et al. also examined the particle diameter. Here they varied the particle diameter from 50 - 300 μm. Fig. 3.7 clearly shows that for diameters smaller than 150 μm resulted in increased erosion rate. Thus, for their study, the critical particle diameter was 150 μm. For small particles, the intense secondary flow in the elbow causes the particles to impact the side wall of the elbow and results in severe erosion. Another theory was that the trajectories of large particles are mainly controlled by inertia force. This will drive the large particle straight and then impact the outer

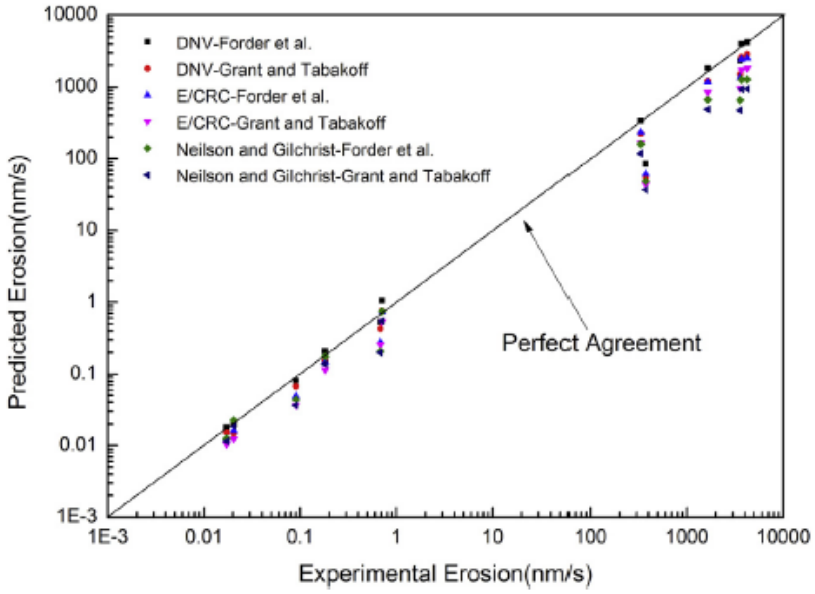

Figure 3.4: Comparison between the predictions using different particle-wall rebound models and the experimental data [56].

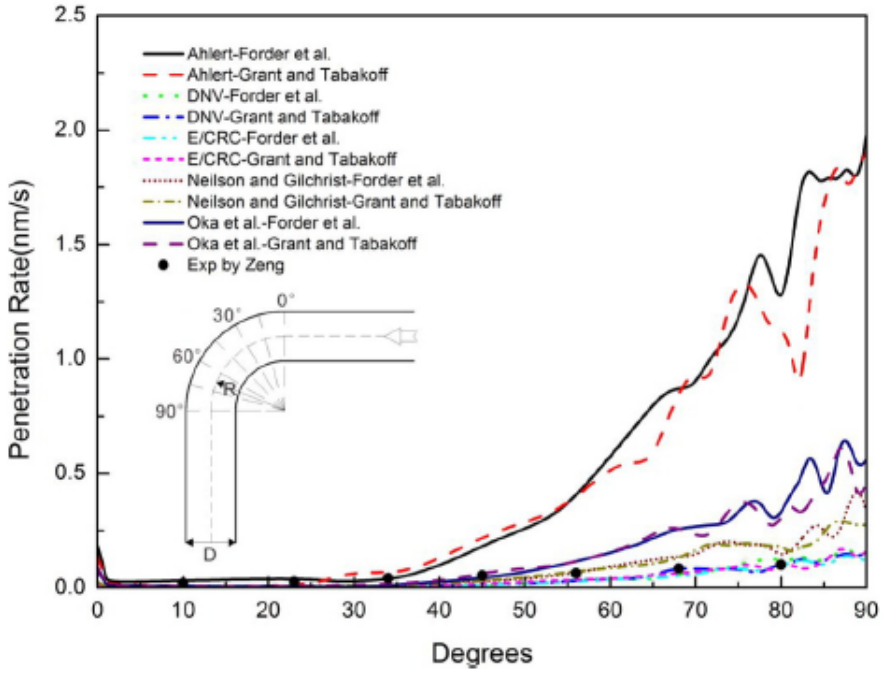

Figure 3.5: Comparison of predicted and experimental penetration rate along elbow curvature angle for five erosion models with different particle-wall rebound models [57].

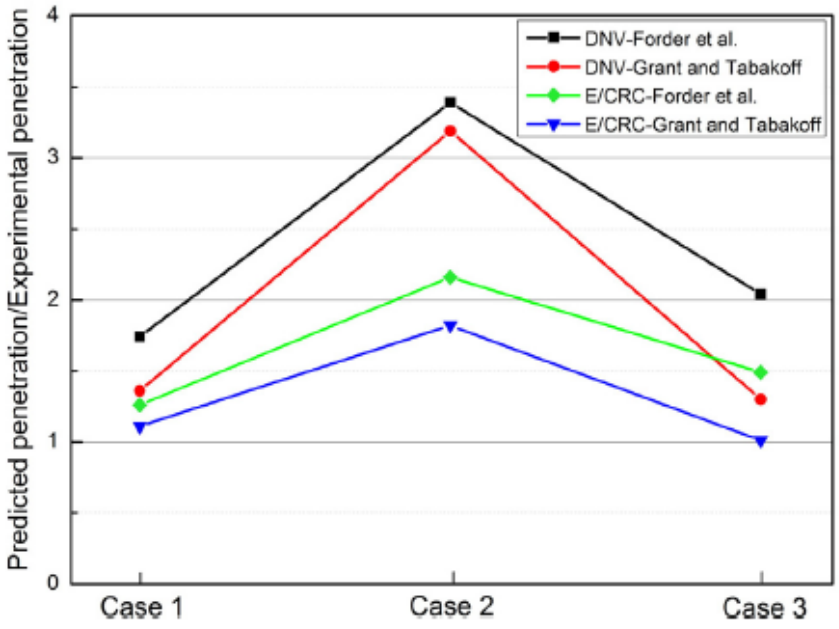

Figure 3.6: Comparison of numerical predictions with experimental data from Bourgoyne [57].

wall at low angles, while smaller particles will impact the wall at larger angles.

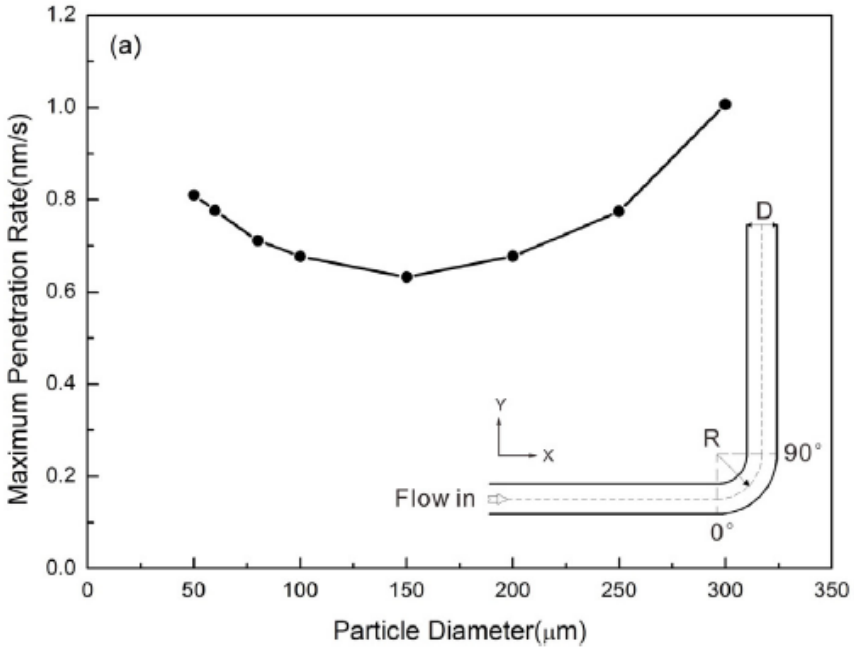

Figure 3.7: Effect of particle diameter on predicted penetration rate [57].

3.3.5 Pereira et al.

In the study by Pereira et al. [59] experimental data collected by Chen et al. [60] was used to compare the simulation results. Four empirical correlations, proposed by Ahlert, Neilson and Gilchrist, Oka et al., and Zhang et al. were investigated. They did a sensitivity analysis regarding the number of computational particles, the restitution coefficient, and of different friction coefficient models. Turbulence was accounted for by the $k - \varepsilon$ model. The four erosion models are shown in Fig. 3.8, where they show the penetration contours. They generated the same contour, but at different angles and penetration rate in the elbow. This was due to the same generated flow field for all the tested models. The highest penetration ratio was observed from the models where the particles impact the bend at maximum velocity. Fig. 3.9 shows the penetration ratio profile for the

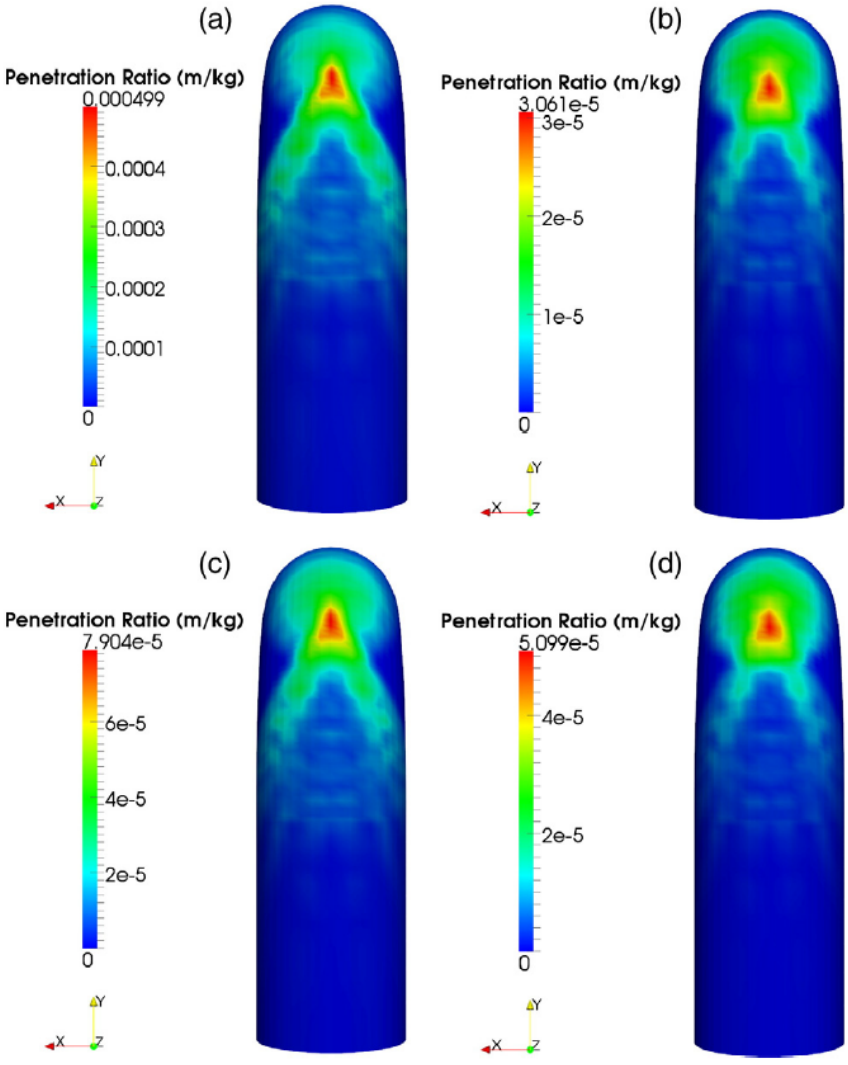

Figure 3.8: Penetration ratio contours for: Ahlert (a), Neilson and Gilchrist (b) Oka (c), Zhang et al. (d) [59].

four simulated models, as well as the experimental data by Chen et al. It can be noticed that the

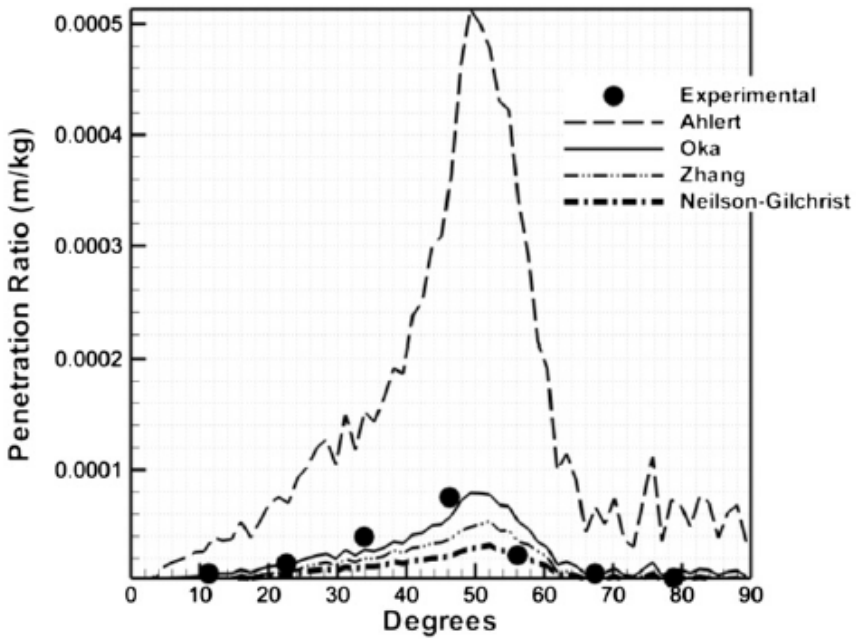

Figure 3.9: Comparison of numerical and experimental penetration ratio versus bend curvature angle for the four erosion models [59].

Ahlert correlation resulted in a higher erosion when compared the experimental results, whereas the other three correlations displayed values closer to the experimental data. The correlations provided by Zhang et al. and Oka et al., gave the best results matching the experiment. Neilson and Gilchrist's correlation showed very low values for the penetration ratio compared to the others. An important conclusion was that all the model predictions were slightly shifted regarding the peak penetration ratio.

3.3.6 Kumar et al.

Kumar et al. [61] studied CFD-based modeling of elbows in series with the particle erosion models by Oka et al., DNV, Grant and Tabakoff, and E/CRC with the Zhang et al. rebound model. They used r/D=1 and obtained an average y^+ value of approximately 7.5. They used $k-\varepsilon$ as turbulence model and E-L method with DPM.

All four models predicted erosion throughout the concave part of the elbow. The erosion rates increased from the entrance up to sweep angle 80° and then decreased towards the exit of the elbow. In their study the erosion profile was not predicted correctly in comparison to the experimental values. All the models achieved the maximum thickness loss at 75°, whereas the experimental peak was obtained at 55°. They found that except the E/CRC models, all the models anticipated thickness loss within +50% of experimental values. The Oka et al. model estimated the thickness loss most accurately although the location of the loss is displaced. They assumed their error to be in the flow prediction or particle-turbulence coupling.

Chapter 4

Methodology

To run a simulation that can represent the actual fluid flow and erosion damage is not straightforward. There are several factors which can affect the results and therefore it is necessary to look at these factors individually.

4.1 Methodology for simulation of erosion

To get a better understanding of the important factors and parameters in CFD-based erosion model, the different steps and their importance are stated in this section.

4.1.1 Geometry and mesh

The geometry was kindly provided by Wintershall Norge AS[1]. The choke valve is positioned so that the inflow is horizontal and the outflow is vertical downwards, see Fig. 4.1. There are several holes of different sizes in the trim. This is to give a smoother velocity profile and even out the ΔP loss when opening or closing the choke valve. The choke valve is an adjustable choke, which means it can change the fluid flow and pressure parameters to suit the process or production the best way possible [62]. This thesis looks into the geometry with a specific positioning of the piston to investigate the erosion with different erosion models and particle size. The choke opening is at 54%.

When the geometry was specified, a mesh for the fluid flow field could be generated. Early in the thesis different *base size* was tested to find the *optimal* mesh size. The optimal mesh is the one where the simulated results are independent of the mesh. The *trimmer* volume mesh, which produces a polyhedral mesh was selected with surface remesher and surface repair. The grid base size was set to 0.001 m after the optimal base size was found. An important note is that a *finer grid gives longer simulation time*. Therefore, a finer grid that provides the same results is less appreciated than the coarser mesh. Particles are added on a later point, see Section 4.1.4.

[1] Confidential data details

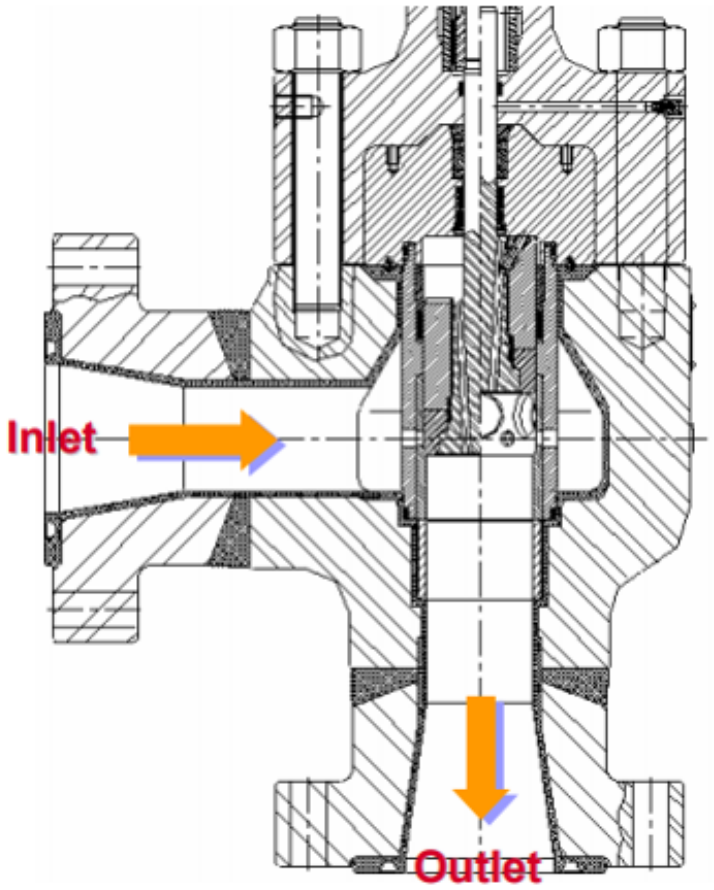

Figure 4.1: 2D geometry sketch of the choke valve plane section.

4.1.2 System description

Erosion and particle-wall interactions were numerically investigated in the three-dimensional choke model. No-slip conditions were specified on the walls of the choke geometry.

As mentioned earlier, the choke investigated in this thesis has an opening of 54%. The piston is the part in the choke which dictates the fluid flow and pressure loss. By changing the location of the piston the choke opening will also change. This can be done inside the modeling phase, here inside the CAD-3D tool. In this specific case, the flow coefficient (CV) calculated at the subsea choke valve to be 33.84±3.81 in US gallons of water at 60°F flowing per minute through the valve with a pressure drop of 1 psi across the valve.

When modeling in CAD-3D, it is the fluid flow volume that is generated. This is where the particles will collide and the erosion can be calculated from the interacting particles. A better picture of the CAD-3D model can be seen in Fig. 4.2a.

(a) (b)

Figure 4.2: (a) Illustration of the choke inlet, where particles are injected. (b) A zoomed illustration of the cage.

4.1.3 Models and solvers

The physical models in STAR-CCM+ decide the behavior of the system investigated, by defining the physical phenomena considered, and by defining the mathematical formulations and conditions. They work together with the solver to obtain a solution. When we simulate CFD-based erosion, we can first run a steady state simulation and let the solvers converge without the Lagrangian phase. After this, we begin to simulate the Lagrangian phase together with the continuous phase. This method was used for the presented results in this thesis.

Another way to simulate the particles is when the steady state velocity flow field is generated, the simulation is stopped. The particles are then run for unsteady state, unlike previously where they were converged and run in steady state. The implicit unsteady solver was primarily used to control and update the simulation at each physical time-step in addition to control the size of each time-step. Before the simulation is run for only the particles, the turbulent flows are removed. The particles will follow the continuous phase and be guided by the velocity throughout the choke volume. The particles will achieve the maximum velocity in the same region as the continuous phase. The overall time consumed by doing the simulation in two steps is less than if the simulation was run with particles and gas from the start. The results are just as detailed when doing two simulations as one, and vice-versa. This method was used for the early stage simulations in this thesis.

Inside the STAR-CCM+ simulation program, there are several models to chose from, where the most important ones are covered in Chapter 3. The most important models and solvers for the continuous phase in this thesis are given in the Appendix.

The Lagrangian multiphase model was selected to describe the dispersed sand phase. The oil flow that occurs simultaneously was neglected in this thesis. The models selected for the Lagrangian phase are given in the Appendix.

The solvers in STAR-CCM+ controls the solution and are activated once per iteration. The models select the required solvers, and different models can use the same solver. As mentioned earlier, in this thesis the particles were injected after the simulation of the continuous phase. The continuous phase then determines how the discrete phase behaves as the particle tracks are recorded in the simulation. The particles were also affected by the Lagrangian modeling methodology, including inter-particle contact forces in the particle equation of motion [5].

4.1.4 Boundary and initial conditions

Boundary conditions are given both for the continuous phase and the dispersed phase, while initial conditions only are given for the continuous phase, see Table 4.1 - 4.3.

Table 4.1: The boundary conditions for the continuous phase

Boundary	**Boundary Conditions**
Inlet	Inlet Velocity
Outlet	Pressure Outlet
Inner Walls	No-slip Wall

Table 4.2: The initial conditions for the continuous phase

Parameter	**Initial Value**	**Unit**
Pressure	0.0	bar
Static Temperature	380	K
Turbulence Specification	$k-\epsilon$	-
Turbulent Dissipation Rate	0.1	m^2/s^3
Turbulent Kinetic Energy	0.001	J/kg
Velocity	[0.0, 0.0, 0.0]	m/s

Table 4.3: The boundary conditions for the dispersed phase at the wall

Physics Condition	
Mode	Rebound
Physics Values	
Impact Wear	DNV/Oka/Ahlert/ Neilson and Gilchrist
Normal Restitution Coefficient	Forder et al./ Grant and Tabakoff
Tangential Restitution Coefficient	Forder et al./ Grant and Tabakoff

There are also *Reference Values*, values from the environment of the system, for the continuous

phase. These were set to match the data of the real choke, provided by Wintershall Norge AS. The reference values are given in Table 4.4.

Table 4.4: Reference values for the continuous phase

Parameter	**Reference Value**	**Unit**
Minimum Allowable Distance	$1.0 \cdot 10^{-6}$	m
Minimum Allowable Temperature	100.0	K
Reference Pressure	175.0	bar
Maximum Allowable Temperature	5000.0	K

4.1.5 Particle injector

In STAR-CCM+, the particles are defined in the Lagrangian phase. Here properties such as material and drag force are adjustable. This phase is inserted into the fluid continuum through *injectors*. The injectors define the direction and the frequency of particle flow into the system. We can choose how the dispersed phase is going to enter the continuous phase. Possible scenarios are that particles may be injected randomly, from a surface or from a specific point. For this thesis, the particle was injected from the *inlet* surface. Fig. 4.3 shows an illustration of the system with particles injected from the inlet.

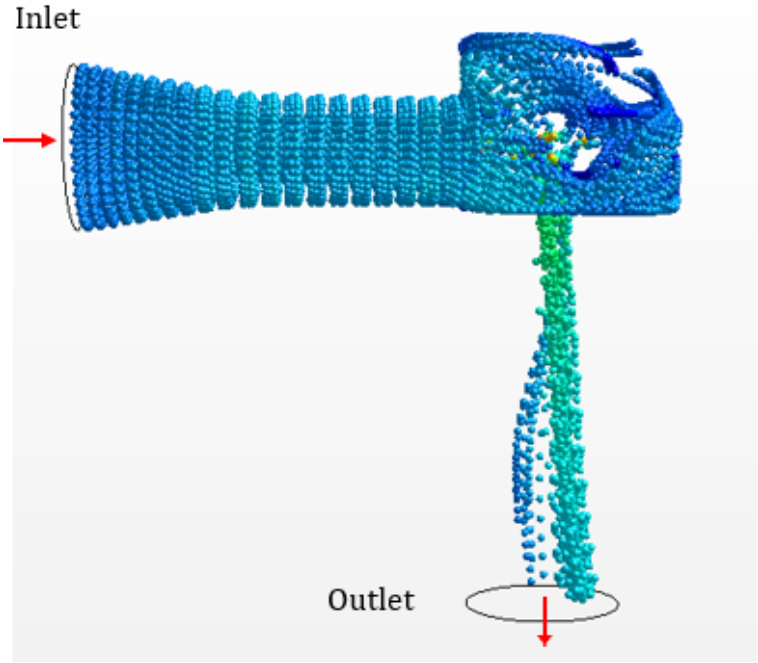

Figure 4.3: Illustration of sand particles injected from the inlet through the choke geometry.

The settings for the particle injector are found in Table 4.5.

Table 4.5: Settings for the particle injector

Conditions		
Flow Rate Distribution	Per Injector	
Flow Rate Specification	Particle Flow Rate	
Particle Size Specification	Particle Size	
Velocity Specification	Magnitude + Direction	
Values		
Point Inclusion Probability	1.0	-
Parcel Streams	3	-
Injection Direction	[0.0, 1.0, 0.0]	-
Particle Diameter	$4.00 \cdot 10^{-7}$ - $4.00 \cdot 10^{-4}$	m
Particle Flow Rate	50.0	s^{-1}
Velocity Magnitude	8.541	m/s

4.1.6 Particle flow

Process parameters for the particle flow are a key selection to get the desired results. It is equally important to give the right input parameters for the dispersed phase and the continuous phase. Small differences can impact the results severely, such as velocity and therefore also the erosion wear. Table 4.6 shows the selected process parameters for the dispersed sand phase.

Table 4.6: Process parameters

Material	**Process Parameter**	**Value**	**Unit**
Dispersed phase	Particle size, d_p	$4.00 \cdot 10^{-7}$ - $4.00 \cdot 10^{-4}$	m
	Density, ρ_d	2600	kg/m^3
	Drag Force, F_D	Schiller-Naumann	-
	Inlet velocity, V_0	8.541	m/s

For the dispersed phase, the particle size was set to $4.00 \cdot 10^{-5}$ m for the initial testing of the different erosion models. Later the particle diameter was changed in order to investigate the influence on erosion wear. Moreover, this was also done for different erosion models. The density of the sand particles was set to 2600 kg/m^3.

4.1.7 Simulation procedure and calculations

First, the simulations were run without particles in the system. The initial velocity was set to zero so that the only influencing parameter at start-up was the velocity inlet boundary. The goal of these first steps was to achieve a steady state velocity profile. The next step was to set the fluid flow to be independent of time and run the particle simulation. The system simulated a one-way coupled multiphase flow, where the dispersed phase does not affect the continuous phase. After injecting the sand particles to the system in the positive y-direction, the particles accelerated through the smaller pipe diameters. Near the walls, the particles decelerated, due to shear and

boundary conditions. Gravity was neglected as the Reynolds number was very high. By simulating the particles without DEM, the effect of rolling along the wall is not taken into account. All of the simulations were set up without DEM, it is assumed no collision between the particles themselves and that the particles only affect the wall by rebound models.

4.1.8 Simplified choke geometry

Form friction losses in the Bernoulli equation are combined with the skin friction losses of straight pipe, Eq. (2.13), to give the total friction loss. The geometry for friction loss will be simplified in this thesis to make the calculations easier since there exists no data on the K_f for this choke geometry. The system was assumed to be a straight pipe with several contraction pipes before expanding back to the original cross-section area and entering a 90° elbow and a new straight pipe of the same initial diameter, see Fig. 4.4. Afterward, we combine all the losses into one common equation for the total friction h_f:

$$h_f = \left(4f\frac{L_1}{D_1}\frac{\bar{V}_{fa}^2}{2} + 4f\frac{L_2}{D_2}\frac{\bar{V}_{fb}^2}{2} + 4f\frac{l}{D_c}\frac{\bar{V}_{fc}^2}{2} + K_c\frac{\bar{V}_{fc}^2}{2} + K_e\frac{\bar{V}_{fc}^2}{2} + K_f\frac{\bar{V}_{fb}^2}{2} \right), \tag{4.1}$$

where the velocity corresponds to the term we investigate.

4.1.9 Post processing tools

STAR-CCM+ is a multi-purpose simulation software with post-processing tools. In order to analyze results from the simulations, scenes, reports, plot, and solution histories can be used.

Scenes were created as visualization displays of geometry, mesh, scalars, and vectors, making it possible to view solution data from either a running or a finished simulation. It is possible to watch a flow field evolve as the simulation iterates, changing some parameters and immediately see the effects of those changes. By creating a solution history, a movie of the scenes can be made for the complete simulation. This also makes it possible to look back at scenes at a given time.

The parameters of particular interest for the current work was the velocity profile and the particle tracks. By first finding a good grid and velocity profile, the particles were ready to run. The particle simulation was run with different erosion models and particle size.

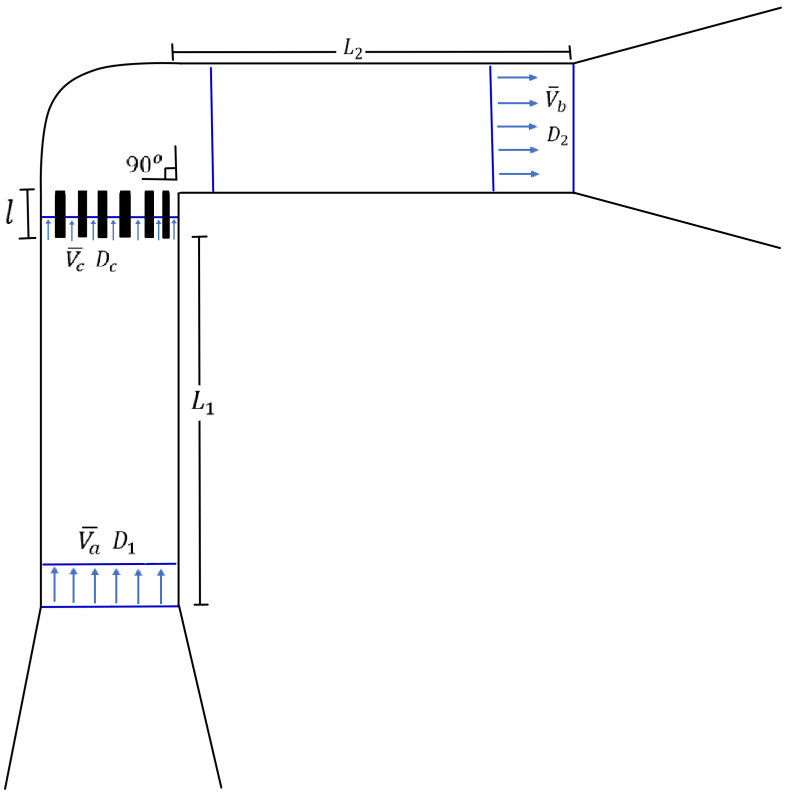

Figure 4.4: Simplified choke geometry.

Chapter 5

Results and discussion

This chapter shows the comparison of different CFD-based erosion models in this thesis, as well as results for different particle sizes. The first section discusses the importance of mesh selection.

5.1 Mesh Selection

Finding an optimal mesh is a key factor to find accurate results using CFD-based analysis. To get the best results the mesh should give close to or the same results on a finer grid. In this thesis, the velocity profile, pressure loss, and y^+ were examined to find the optimal grid. The selected *mesh solvers* are shown in Table 5.1 [5].

Table 5.1: Mesh solvers selected for different meshes

Mesh Nr. 1-3	**Mesh Nr. 4**
Surface Remesher	Surface Remesher
Automatic Surface Repair	Automatic Surface Repair
Polyhedral Mesher	Prism Layer Mesher
Thin Mesher	Trimmed Cell Mesher
Prism Layer Mesher	

It is important to note that the prism layers were used to resolve the boundary layer. Without it, values for the fluid and particles near the wall could be erroneous.

The *Process Parameters* were changed for different meshes. Here the main difference between the different meshes was the number of cells generated by the meshers. The coarsest mesh had a base size of 1.2 cm, where the remesher automatically decreases the cell size at finer geometry parts. Table 5.2 shows the different meshes and their number of cells.

Looking at the values of y^+ wall, Table 5.2, it was clear that the meshes in Nr. 1, 2 and 3 did not give satisfactory results. Their y^+ values were over 800 which is outside the regimes stated in section 2.3.7. Furthermore, mesh Nr. 1 was not selected as the geometry became deformed at the outer cage due to the coarse base size, resulting in a sharp edge where there should have been a smooth surface. To reduce the y^+ values the mesh has to be finer. This led to the selection of

Table 5.2: Mesh results

Mesh	**Process Parameter**	**Value**	**Unit**
Nr. 1	Base size	1.2	cm
	Nr. of cells	194 406	-
	Inlet velocity, V_0	8.541	m/s
	Maximum velocity, V_{max}	131.10	m/s
	Pressure loss, ΔP	10.38	bar
	Average y^+	806	-
Nr. 2	Base size	1.0	cm
	Nr. of cells	234 789	-
	Inlet velocity, V_0	8.541	m/s
	Maximum velocity, V_{max}	128.28	m/s
	Pressure loss, ΔP	9.965	bar
	Average y^+	806	-
Nr. 3	Base size	0.5	cm
	Nr. of cells	485 070	-
	Inlet velocity, V_0	8.541	m/s
	Maximum velocity, V_{max}	131.01	m/s
	Pressure loss, ΔP	9.679	bar
	Average y^+	806	-
Nr. 4	Base size	0.1	cm
	Nr. of cells	3 168 302	-
	Inlet velocity, V_0	8.541	m/s
	Maximum velocity, V_{max}	131.10	m/s
	Pressure loss, ΔP	8.679	bar
	Average y^+	73.0	-

Nr. 4, with over 3 million cells. Here the y^+ values are satisfactory. The values for the maximum velocity and the pressure loss are very similar to each other, which is a good indication for optimal mesh selection. The velocity profile is finer and more defined, due to the smaller grid cells which will be discussed further at a later point. However, due to the number of cells, the simulation time increased.

The simulation of the fluid flow was run in four steps to achieving convergence. In the first step, the simulation was run without the energy equation. In the second step, the computation was performed without simulating the fluid flow where the energy equation was converged alone. In the next step, the energy equation was not used again and the objective was to stabilize the flow field. The aim of the last step was to converge the flow with the energy equation solver. This simulation was done on a computer with 15 cores to speed up the computational time spent. This simulation differed from simulations on mesh Nr. 1-3 where only four cores were used.

5.1.1 Flow modeling

The first step in prediction the erosion process using CFD was to find the fluid flow field profile and velocities. The gas was simulated alone before the particles were injected. The enabled models are shown in Table A.1.

The gas properties in a simulation are one of the key parameters to make the simulation as accurate as possible. For this Wintershall Norge AS provided the gas data needed, but is not given in detail in this thesis[1].

By comparing the maximum velocity of the different meshes we can see that they are close to each other, see Table 5.2. Furthermore, all the flow profiles gave the highest velocities in the same area, namely in the smallest holes in the choke. This corresponds to the equation of continuity, which states that for smaller pipe diameters, the velocity will increase. This is illustrated in Fig. 5.1.

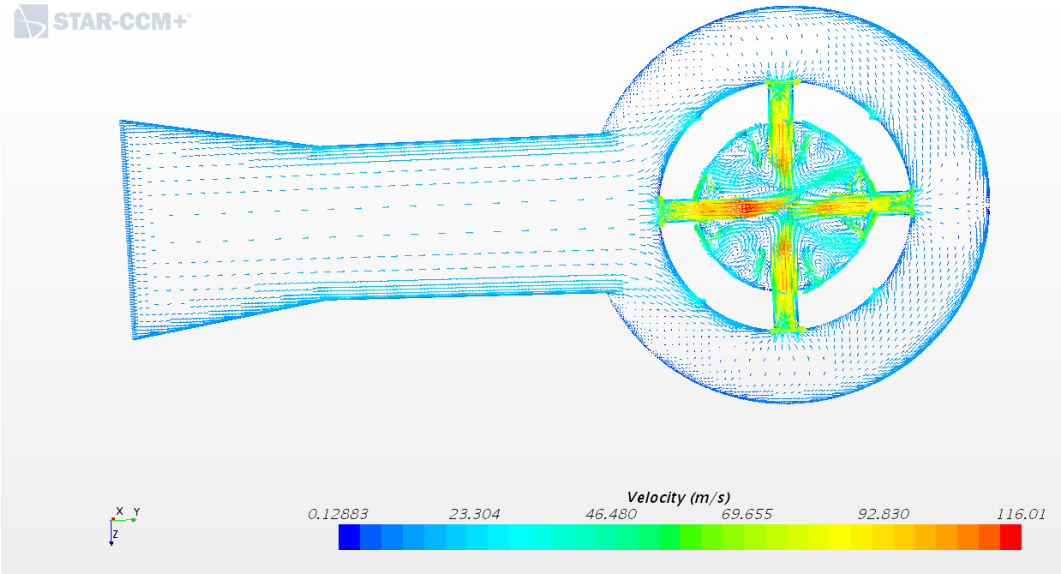

Figure 5.1: Illustration of the gas velocity profile inside the choke geometry, where the inlet is to the left and the holes leading towards the outlet is on the right.

According to the simulations, the maximum velocity for the continuous phase was 126.16 m/s. The dispersed phase was not able to achieve a higher velocity than the maximum velocity of the gas.

Fig. 5.2 shows the gas flow comparison for the different meshes. All the meshes show the same tendency, the main flow is highest through the trim holes and the flow follows the right side through the outlet. The fact that the flow profiles are very similar is a good indication for accurate results.

5.1.2 Pressure loss

Pressure loss, ΔP, was also looked upon when choosing the right mesh, see Table 5.2. The pressure drop was calculated by finding the difference between the pressure at the inlet and at the outlet.

[1] Confidential data

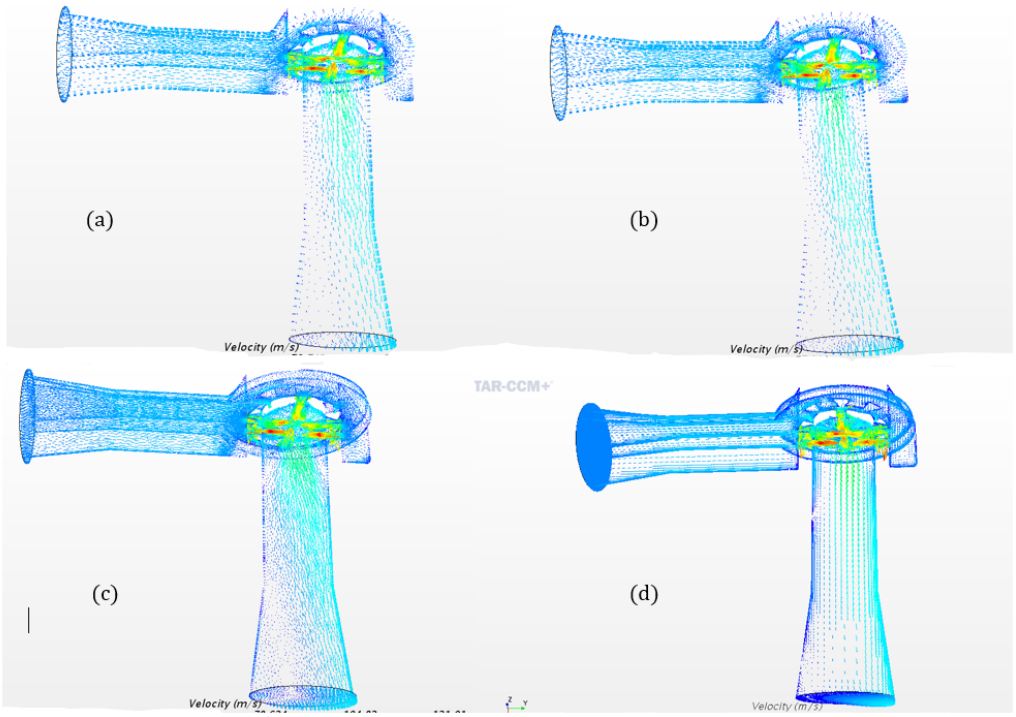

Figure 5.2: Fluid flow field for different meshes. (a) represents mesh Nr. 1, (b) Nr. 2, (c) Nr. 3, and (d) Nr. 4.

This was calculated at each iteration. This was also used as another indication of convergence: it was expected that the pressure loss stabilized.

When choosing the right mesh size, the pressure drop should be the lowest at the most accurate mesh size. This indicates that mesh Nr. 4 is the optimal one as it results in the lowest pressure drop in the examined simulations.

5.1.3 Particle motion

The second step in predicting erosion rate is determining particle motion. The particles were run in one step, together with the turbulence models enabled. In this step, several sub-steps were made to make sure the final result of the single step was correct. The particle tracks are shown in Fig. 5.3. Here we also see that the particles almost achieve the same velocity as the carrier fluid, 131.10 m/s, and that the dispersed phase follows the carrier flow as shown in 5.2. Moreover, the particles obtain maximum velocity where the continuous phase does.

By examining Fig. 5.4 there are clearly several places where the particles move inside eddies. These places, where the particles swirl is investigated further in the following section.

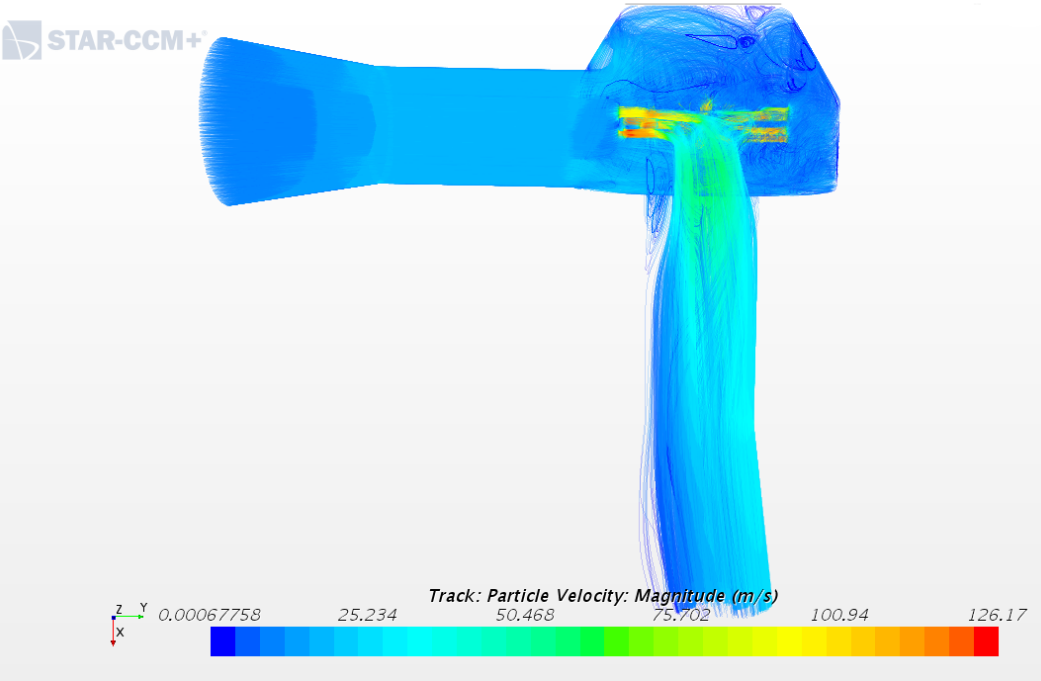

Figure 5.3: Illustration of the transparent particle track inside the choke geometry.

5.2 Erosion results

Finally, the third step was calculating the erosion from the particle track. The particle motion in the simulation was run as steady for a single step. During that step, the model tracked each individual particle. In STAR-CCM+ the erosion was calculated at the same time the simulation was run. Different parameters were changed to look at the effect of erosion wear, namely erosion models and particle size.

5.2.1 Erosion model comparison

In this thesis, four erosion models were tested for simulations where particles of sand were injected into the choke volume at the rate of 50 particles per second. The particles had a size of $4.00 \cdot 10^{-5}$ m. The erosion models and their overall erosion rate are given in Table 5.3. The overall erosion rate is the erosion rate for the entire choke valve.

Table 5.3: Erosion Models and Overall Erosion Rate Results

Erosion Model	**Overall ER**	**Unit**
Oka et al.	$2.39 \cdot 10^{-7}$	g/hr
DNV	$2.25 \cdot 10^{-7}$	g/hr
Nelson and Gilchrist	$1.20 \cdot 10^{-7}$	g/hr
Ahlert	$1.95 \cdot 10^{-5}$	g/hr

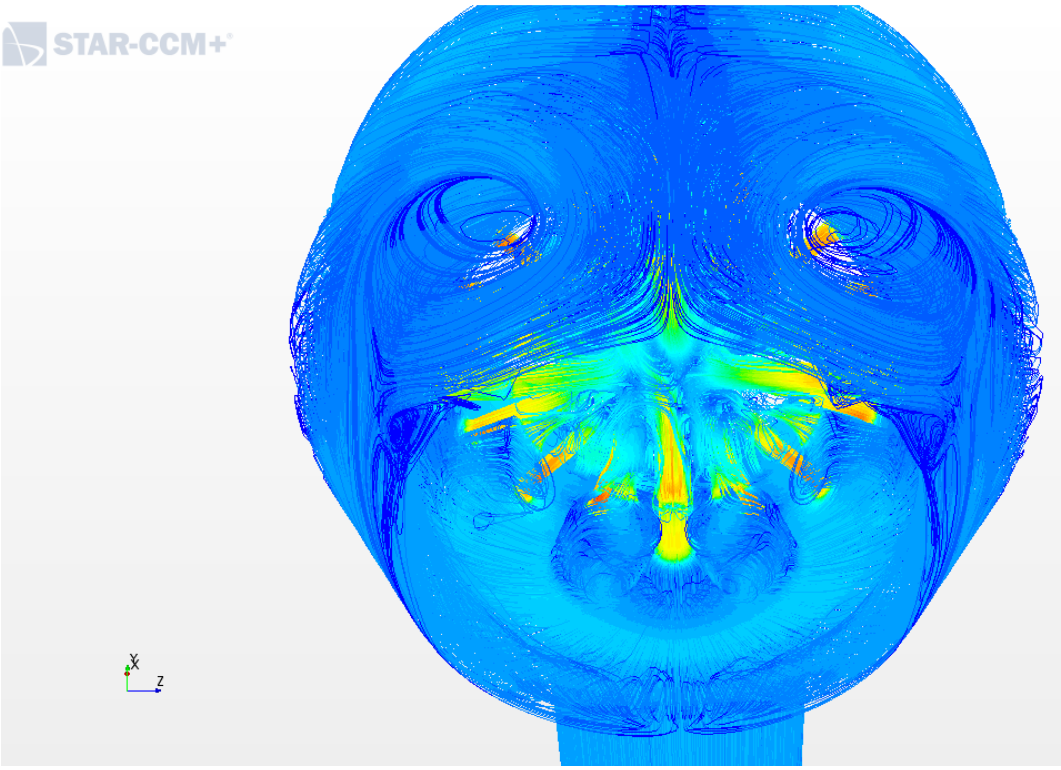

Figure 5.4: Illustration of the particle track inside the choke geometry, from behind.

According to Table 5.3, the Oka et al. model gives the lowest overall erosion rate while the Ahlert model results in the highest overall erosion rate. The reason for the much higher erosion results using the Ahlert correlation is that STAR-CCM+ default settings are for liquid-borne semi-rounded sand particles eroding aluminum. The Nelson and Gilchrist correlation is also for liquid-borne sand, but eroding AISI 4130 steel, which results in less erosion than for aluminum. The DNV and Oka et al. models are both for air-borne sand eroding carbon steel, thus giving less erosion and the most accurate results for this thesis.

By comparing the results to the ones obtained by other researchers mentioned in Chapter 3, it is clear that the Oka et al. and DNV model are reliable models for gas-solid flow. Pari et al. [53] found that the Oka et al. model resulted in higher erosion rates than when using the DNV, and Neilson and Gilchrist models but that they all underpredicted the erosion damage on the examined pipebend. Vieira et al. [47] concluded that the Oka et al. model showed a very good agreement with the experimental results while the Neilson and Gilchrist, and DNV models underpredicted the erosion damage by a range between 2-10 %. Zhang and Liu [49] found that the Oka et al. and DNV model gave very similar results in erosion prediction, but that they both overpredicted the erosion damage. In their results, the DNV model gave better results than the Oka et al. model. Pereira et al. [59] concluded that the Oka et al. model showed a very good agreement with the experimental results, while the Neilson and Gilchrist model underpredicted and the Ahlert model overpredicted the erosion rate significantly. Peng et al. [56] found that the DNV erosion model together with the Forder et al. particle-wall rebound model produced the most accurate result for gas-solid flow. Here the Neilson and Gilchrist erosion model underpredicted the erosion damage.

5.2.2 Particle size

When analyzing at the effect of the particle size effect on erosion damage, several researchers have analyzed the process for 90 degree bends and pipelines. However, only a handful of researchers have studied erosion in choke valves [1, 40].

In this research, the number of particles injected into the control volume of the choke was kept constant for all the simulations. The results can be seen in Fig. 5.5. The model by Oka et al. was used for particle size sensitivity.

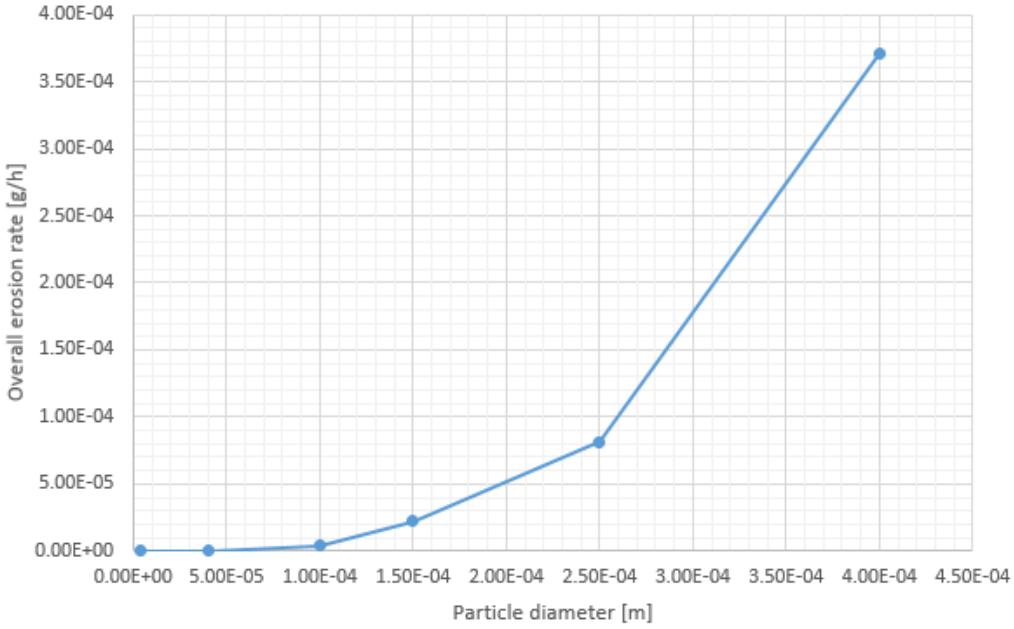

Figure 5.5: Particle size effect on overall erosion rate.

Researchers who have studied the erosion of different particle sizes in bends discovered that at for diameters smaller than some critical value, the erosion rate increased, see Peng et al. [57] and Fig. 3.7. The main explanation is that the smaller particles are more heavily affected by the turbulence and eddies inside the pipebend. By studying the particle flow inside the choke geometry we observed that there were no eddies in the throttle holes, where the erosion rate was the highest. In this research, the overall erosion decreases when the particle size decreases. Therefore, there was no critical particle diameter for this geometry. However, it was interesting to see if the erosion in other parts of the choke is affected by the smaller particles injected.

To support the theoretical analysis, Fig. 5.6 clearly shows that trajectories of smaller particles show more intense swirling inside the choke geometry than for bigger particles. Furthermore, this also affects the erosion as shown in Fig. 5.7 - 5.9.

Fig. 5.7 used a finer erosion rate scale than Fig. 5.8 and Fig. 5.9 to elucidate the erosion process. Despite the differences in scale, there is no erosion wear in the regions indicated by the dark blue zones for any of the figures.

Figs. 5.7b.1 and 5.7b.2 show interesting results: unique erosion patterns were created by the small particles, while the erosion pattern tendency for larger particles was the same. This shows the

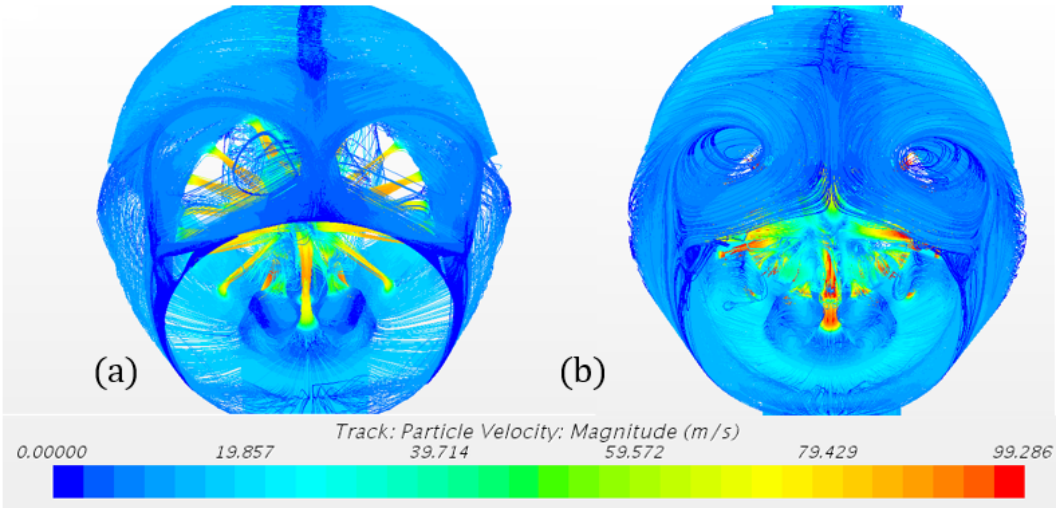

Figure 5.6: Particle tracks for (a) d_p=1.50 · 10^{-4} m and (b) d_p=4.00 · 10^{-6} m.

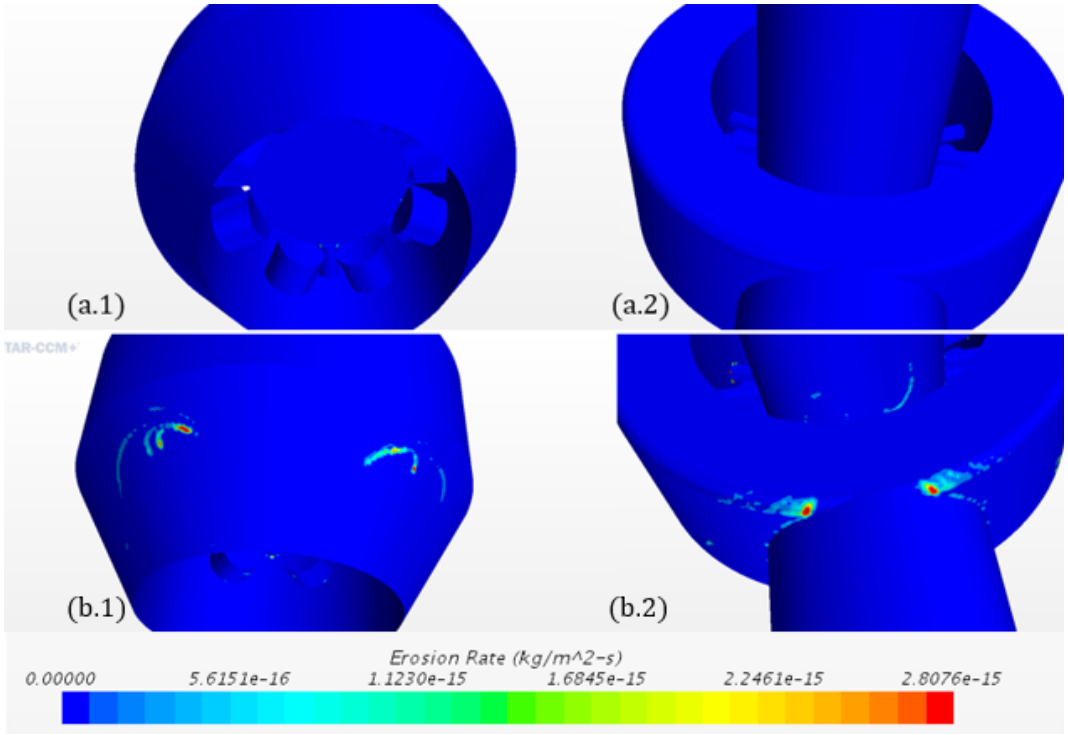

Figure 5.7: Erosion rate of the choke valve in a scalar scene, where 1 indicates the back of the choke and 2 indicates the front of the choke. (a) shows the particle size d_p=4.00 · 10^{-7} and (b) d_p=4.00 · 10^{-6}.

dependence of the erosion rate is on particle size and the turbulence of the continuous phase. It could, therefore, be important to estimate the size of debris coming up from the formation during production.

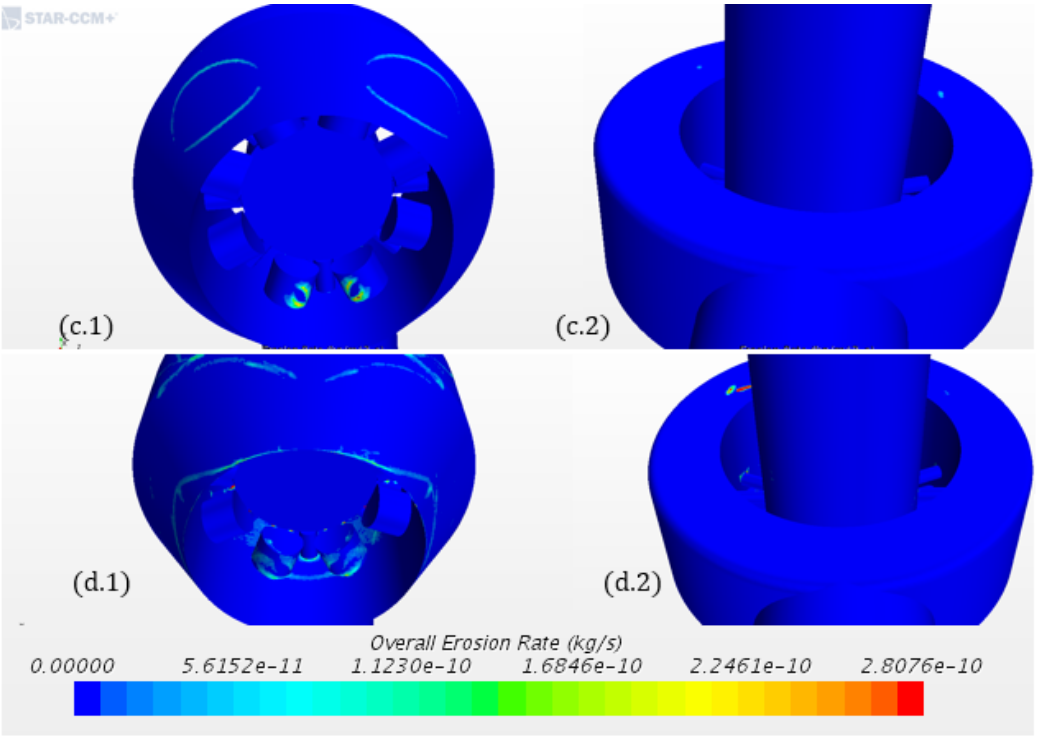

Figure 5.8: Erosion rate of the choke valve in a scalar scene, where 1 indicates the back of the choke and 2 indicates the front of the choke. (c) shows the particle size d_p=4.00 · 10^{-5} and (d) d_p=1.00 · 10^{-4}.

Thus, as the particle tracks differ for different particle sizes, the erosion rate profile differs. It is also clear to see that bigger particles cause greater erosion damage. The smaller particles give less overall erosion damage, this is due to the main flow coming from the inlet. The flow with particles will first hit the cage before either entering the cage holes or slow down and flow around the choke valve. Fig. 5.10 shows the erosion profile for the flow as seen from the inlet in the positive Y-direction, to the holes leading towards the outlet. Here most of the erosion takes place in all the examined cases. This could be another reason why the overall erosion never increases with smaller particles, as some researchers have observed for 90 degree bends.

During oil and gas production the amount of debris of different sizes flows through. However, the amount of debris is neither constant in terms of particles flowing through, nor the mass flow rate. Due to this, the number of particles per second was chosen as the constant flow rate for the main study in this thesis. On the other hand, simulations were also run for a constant mass flow rate at 1.74 · 10^{-5} kg/s, see Fig. 5.11. Here the simulations show a tendency for lower overall erosion rates for smaller particles. This is a good verification of the results achieved from the constant particle flow rate. For particle diameters of 1.50 · 10^{-4} m, there is a local maximum overall erosion rate. This could be due to the turbulent eddies or secondary flows. The local minimum obtained in these simulations could be the same as the critical value Peng et al. found. The smallest particle diameter Peng et al. tested was 50 μm, so there could be a further decrease in the erosion rate for even smaller particles. The figure shows that for even bigger particle diameters the erosion increases approximately linearly. However, the mass flow rate for these simulations is very high and would damage the valve within 24 hours with erosion rates of 7.2 kg/h for the bigger particle

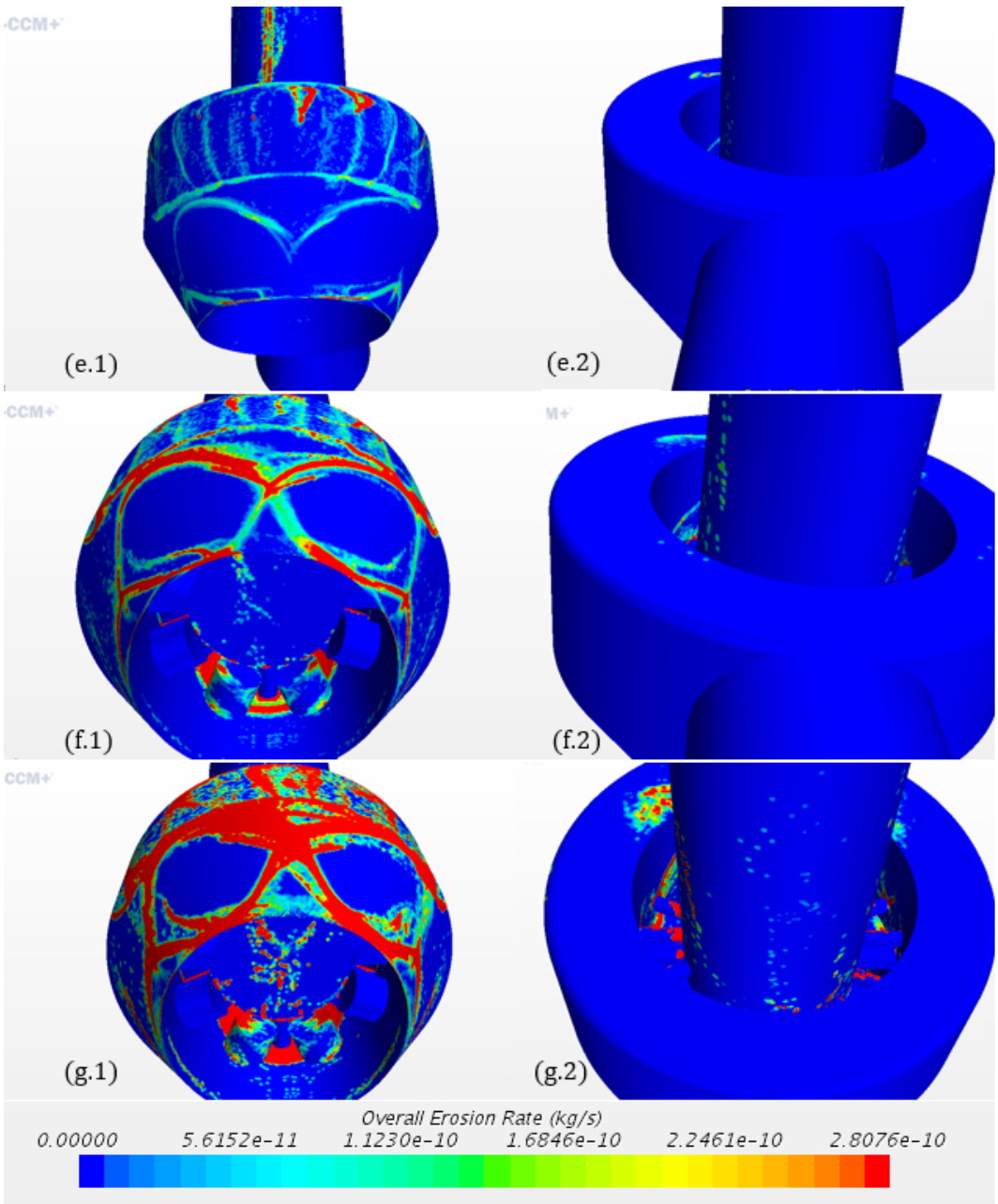

Figure 5.9: Erosion rate of the choke valve in a scalar scene, where 1 indicates the back of the choke and 2 indicates the front of the choke. (e) shows the particle size d_p=1.50 $\cdot$ 10^{-4}, (f) d_p=2.50 $\cdot$ 10^{-4} and (g) d_p=4.00 $\cdot$ 10^{-4}.

diameters. On the other hand, when the valve is partially eroded, the channels expand so that the mean velocity reduces and this would drop down the erosion rate. The data for constant mass flow rate and overall erosion can be found in Appendix B.

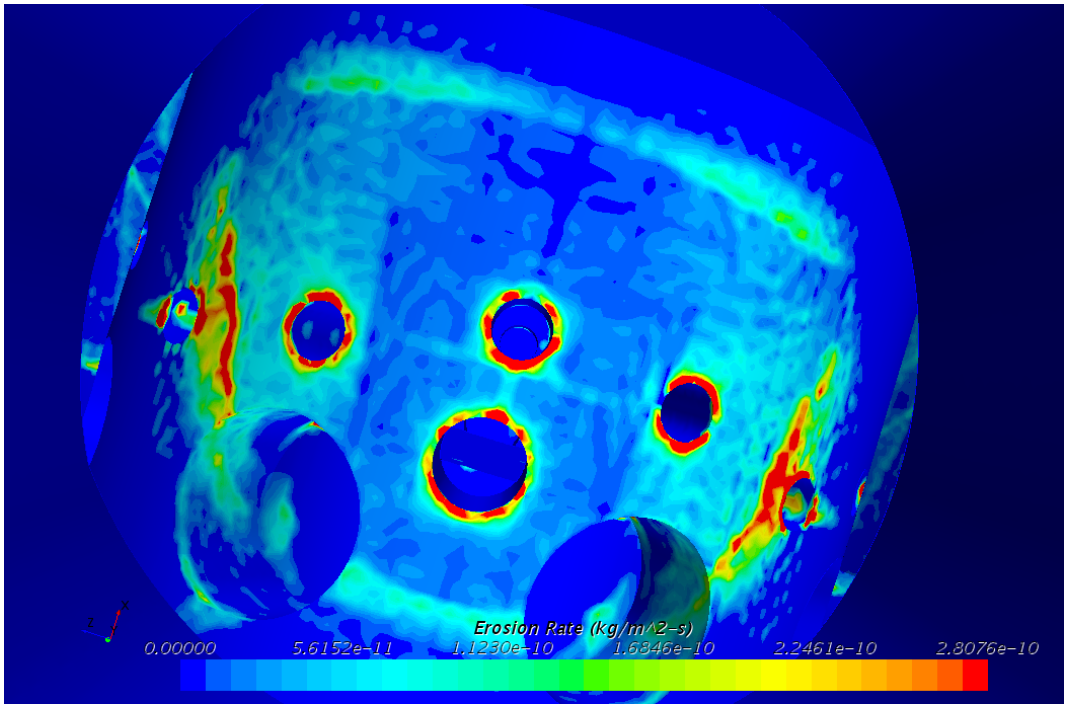

Figure 5.10: Erosion rate and profile as seen from the inlet in the positive Y direction.

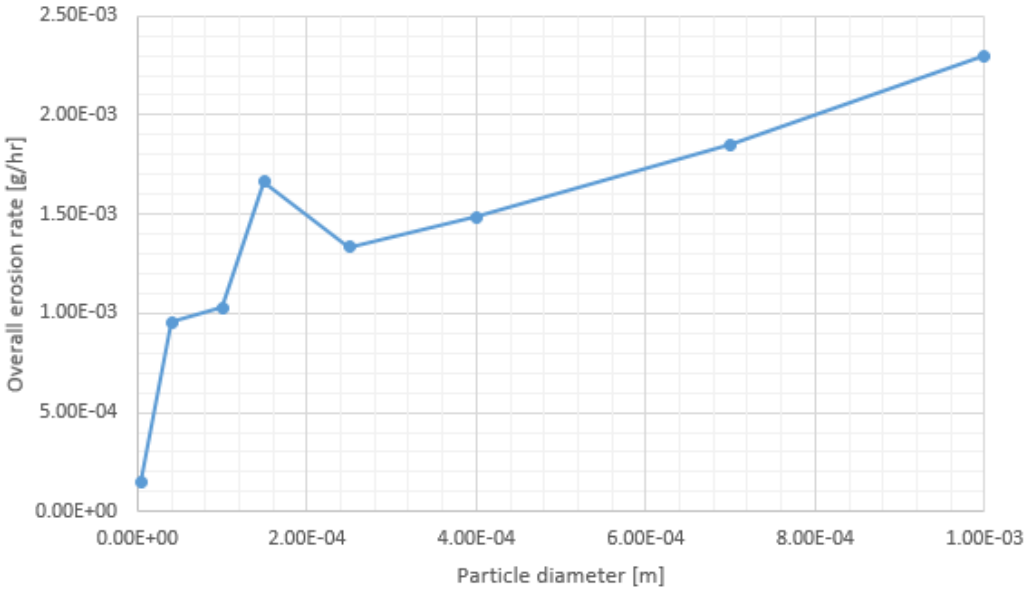

Figure 5.11: Overall erosion rate with a constant mass flow rate at $1.74 \cdot 10^{-5}$ kg/s.

5.2.3 Erosion rate and rebound models

The coefficient of restitution is an indication of the kinetic energy being lost due to rotational kinetic energy, plastic deformation, and heat. For the best-suited erosion model, two different particle-wall rebound models were tested, namely Grant and Tabakoff, and Forder et al. Fig. 5.12 shows the overall erosion for the Oka et al. erosion model and the DNV erosion model with the two particle-wall rebound models. Here the Forder et al. rebound model predicted the lowest erosion result, while the Grant and Tabakoff rebound model resulted in the highest erosion rate. This is the opposite of the results obtained by Peng et al. [57]. The difference in the results is most likely due to the fact that Peng et al. examined the erosion rate for liquid-solid flow for their results. However, the results are closer to each other for smaller particles, than they are for bigger particles. A complete overview of the overall erosion for the different particle sizes, erosion models and particle-wall rebound models can be found in Appendix B.

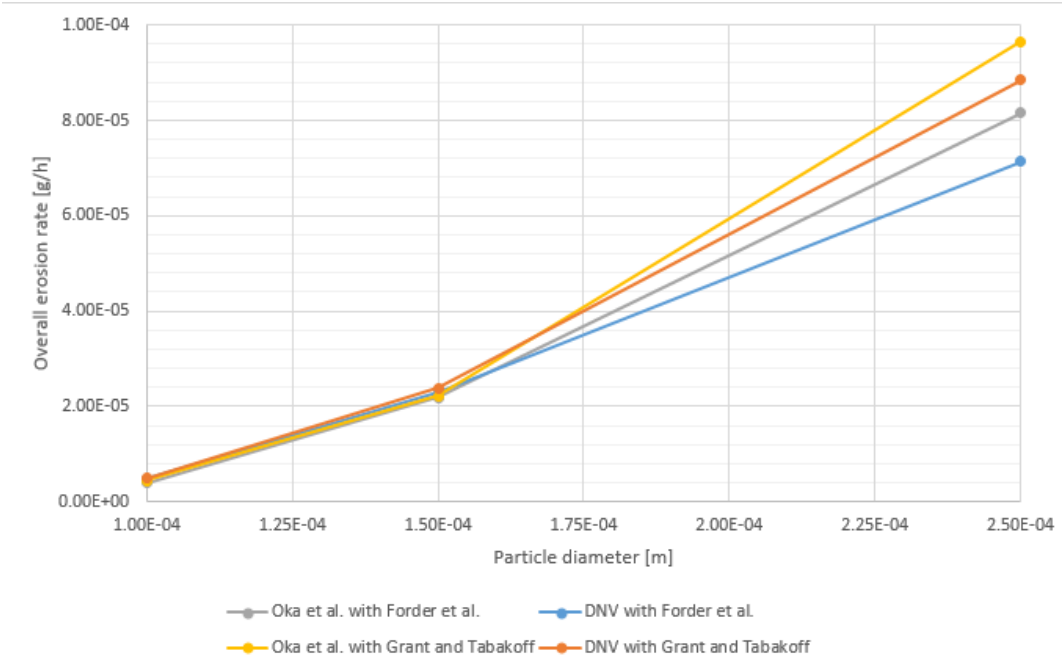

Figure 5.12: Overall erosion rate with two erosion models and two particle-wall rebound models for different particle sizes.

An analysis of the constant particle-wall rebound coefficient was also investigated together with the Oka et al. erosion model. The results are shown in Fig. 5.13. These results give a better understanding of how much the particle-wall rebound models affect the erosion process. The Grant and Tabakoff rebound model resulted in higher values of the overall erosion rate than any of the constant particle-wall rebound coefficients, while the Forder et al. rebound model gave results close to the constant rebound coefficient of 1.0. This indicates that the Forder et al. rebound model was the best-suited rebound model for this study. The results are provided in Appendix B.

According to the simulations, particles that have the same velocity before and after colliding with a wall, rebound coefficient of 1.0, have higher erosion rates than those who have lower particle velocity after collision. This is also shown for different particle sizes in Fig. 5.13. However, the Grant and Tabakoff rebound model gives higher erosion rates, which does not support the

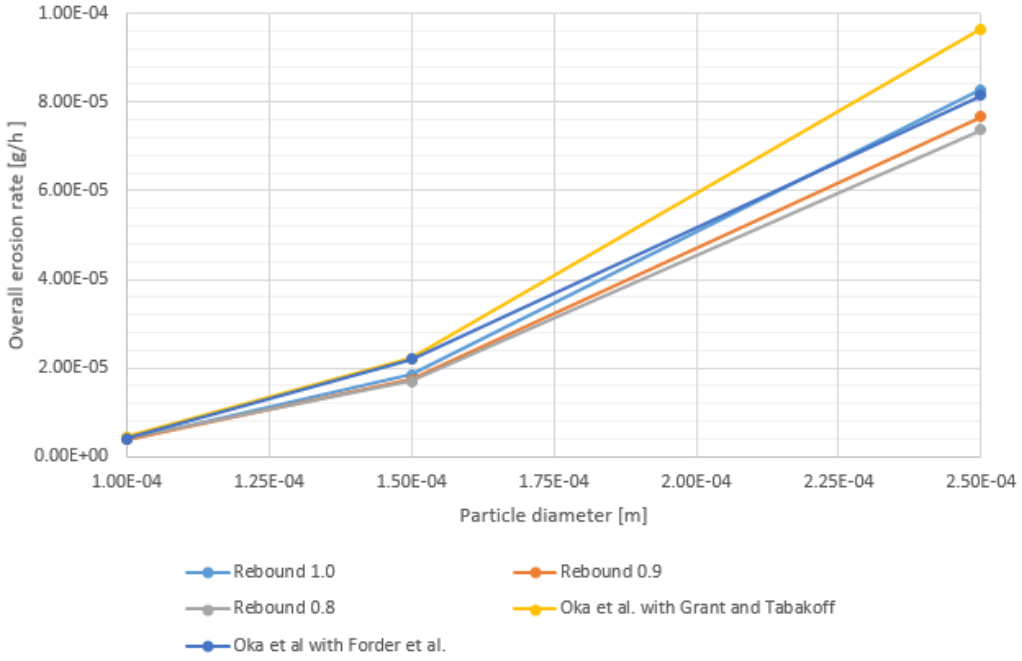

Figure 5.13: Overall erosion rate with Oka et al. erosion model and constant rebound coefficients together with two rebound models.

expressions. Particles are not supposed to accelerate after hitting a wall, thus the lowest erosion results from the empirical rebound models provide the best erosion wear predictions in this study. On the other hand, due to the complex geometry of the choke, it was not possible to exclude the possibility that it is possible to achieve higher erosion rates than those of the rebound coefficient of 1.0.

Furthermore, when we have a lower coefficient of restitution, some of the kinetic energy is lost, the next collision would become weaker. This would indicate that lower rebound coefficients result in lower erosion. However, lower particle velocities right after particle-wall impact could be accelerated by the fluid flow. Then the kinetic energy to the particle would be restored before a new collision. This would be most likely for smaller particles. Another theory could be that after a collision the particles that lose kinetic energy are unable to bounce back into the carrier flow. Then the particles are pushed back into the wall several times with lower kinetic energy after each impact, and therefore give lower erosion rates than for particles with a high rebound coefficient. The particles with a higher rebound coefficient bounce back into the carrier fluid flow and impact the wall with the same velocity multiple times.

5.3 Analytical pressure loss

The analytical pressure loss was calculated by the empirical relations shown in Eq. (4.1). By calculating the pressure loss analytically it is easier to compare it to the data provided by Wintershall Norge AS and the simulation results. The calculated pressure loss over the choke geometry during production at 175.00 bar was calculated to be 48.23 bar, and an overview over the calculated pressure losses at different pressures is shown in Table C.1.

By making a plot of the pressure losses we can see that the pressure loss is approximately linear by increasing pressure, see Fig. 5.14. The point plotted at 100.00 bar deviates slightly from the other points, and the reason for this is most likely that the density was only approximated and not obtained by measurements. In the model, the choke geometry was simplified, since the friction loss coefficient was not predicted for the geometry of the choke studied in this thesis. The results were satisfactory for the simplified choke valve. Wintershall Norge AS provided data for pressure loss over a larger part of the choke valve and pipeline with a pressure drop of 69.06 bar at 175.00 bar and approximately 100°C. The difference in ΔP is acceptable, as the geometry and the length of the calculated area differ.

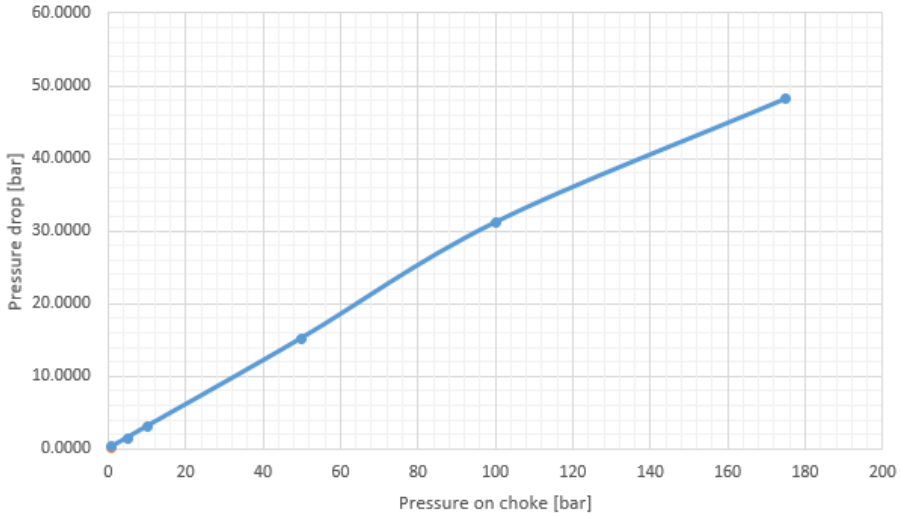

Figure 5.14: Pressure drop at different pressures on the choke.

As shown in Table 5.2, STAR-CCM+ simulation program estimated the pressure loss to be 8.68 bar, which is much lower than both the measured and analytically calculated pressure drop. The main reason for the big gap in the simulated pressure drop is due to the real gas model. This model does not provide the fluid a specific density, however, it has molecular weight, critical temperature, and pressure, as well as specific heat and thermal conductivity. With these parameters, STAR-CCM+ computed a higher density than the measured density by Wintershall Norge AS, and should, therefore, have given higher pressure drop calculations. The reason for this is not known, but it could be due to the selected gas model or a too coarse mesh if the y^+ approaches 1 then the pressure drop could be estimated more correctly.

Chapter 6

Concluding remarks

In this thesis, a mesh with over 3 million grid cells was used for numerical investigations of erosion wear on a choke valve. A multiphase flow system was investigated with the use of the Lagrangian approach to simulate sand particles. Erosion wear is an important parameter when estimating the lifetime and to optimize assets in the oil and gas industry. This chapter presents the conclusions of this study.

When the four different erosion models were tested, two of them were further analyzed with different particle-wall rebound models, and Oka et al. erosion model was tested with different values of coefficient of restitution. The Forder et al. particle-wall rebound model gave the best result together with both the Oka et al. erosion model and the DNV erosion model. However, some of the results with the Oka et al. erosion model with the Forder et al. rebound model resulted in a higher overall erosion rate than for the case when the rebound coefficient was 1.0. This indicated that the DNV erosion model, which yielded the lowest overall erosion, was the best-suited erosion model for this study.

An interesting result from this research was the erosion pattern when different particle sizes were tested. The particles clearly followed the turbulent eddies inside the geometry. Smaller particles were more affected by these eddies than larger particles. Furthermore, this created unique patterns for the particles and, therefore, erosion occurred at different places when the particles were of different diameters. Moreover, since the turbulent eddies inside the choke geometry investigated in this thesis had low velocities, the erosion wear caused by smaller particles had little significance on the erosion wear compared to the erosion wear caused by bigger particles.

According to the simulations, bigger particles cause more erosion wear. This study did not find a critical particle size where the erosion rate increased with smaller particles. However, there was found a local critical particle size which corresponds to the critical size found by Peng et al. The continuous phase, through the trim holes, had high velocity and did not form eddies on the way out towards the outlet. Thus, bigger particles cause higher erosion damage on the wall than smaller particles impacting the same wall. This was verified with both constant particle flow rate and a constant mass flow rate.

In this thesis, the pressure loss was also examined. The results from STAR-CCM+ deviated by a factor of eight from the actual values measured on the real choke valve. An analytical study with a simplified choke geometry gave much better results when compared to the measured values. The measured pressure drop of the choke valve was over a bigger area than the simulated choke valve. This makes the difference tolerable. Thus, the higher approximated pressure drop is more reliable

than the pressure drop results from STAR-CCM+.

In this complex choke valve the highest erosion wear occurs at the cage and cage holes leading towards the outlet that faces the inlet, see Fig. 5.10. Here the main flow impacts the walls and holes directly, before either following the flow through the trim holes or flows around inside the cage. Because the particles follow the main flow, the particles collided with this wall. This makes it possible to look further into the geometry and chose the right material for the choke valve parts. Furthermore, this could lead to choke valves with optimal lifetime.

Chapter 7

Further work

This chapter discusses the identified opportunities and suggestions for further work.

There are several opportunities for further work. In this study, the choke valve had an opening of 54%: therefore, other openings should also be investigated. Different piston placement will provide different flow profiles and values of pressure loss. To understand the erosion wear significance of the piston positioning better for this choke valve, these investigations are necessary. Furthermore, there are several choke valves that vary in size and geometry. For that reason, these investigations are important. The exact measurement data from Wintershall Norge AS was only provided for the choke opening of 54%, which is why the choke geometry was kept constant in this study.

As mentioned under *Results* the final mesh of 3 million grid cells could have been made even finer to control if there were other more optimal meshes. Sensitivity studies of finer meshes will make it possible to govern the y^+ values and the pressure loss.

In this thesis, gas was the continuous phase. For a better understanding of the erosion in choke valves, different fluids should be examined. The turbulent eddies and the flow profile will be different for other fluids compositions. The erosion models by Neilson and Gilchrist, and Ahlert tested for this study, gave an indication of the erosion results for liquid-solid flow. However, these are not accurate enough as the continuous phase for this study was gas and not liquid. Therefore, it would be interesting to look at liquid-solid flows with different fluid compositions and other gas compositions.

The fluid flow velocity in this thesis was set to match the velocity in the choke valve provided by Wintershall Norge AS. By changing the fluid velocity, the flow profile would change. Thus, giving other erosion imprints on the choke valve. Researchers have found that increasing velocity increases erosion rate, therefore, it could be interesting to see if it is possible to obtain the same results.

STAR-CCM+ did not calculate the pressure loss correctly. The real gas model in STAR-CCM+ calculates the density from the molecular weight, critical pressure, critical temperature, specific heat, thermal conductivity, and dynamic viscosity. This resulted in a higher calculated density than the provided density used for the analytical pressure loss. Thus, the calculated pressure drop should have been higher. The use of other gas models is a possibility for further work to see if STAR-CCM+ can calculate more accurate pressure losses. Another option is to try different boundary conditions. The simulations in this study used *pressure outlet*, while other options such as *outlet* could have been used. On the other hand, the ΔP deviation could be due to the approximation

to single gas phase, when in reality it was a multiphase flow for the continuous phase. This has an impact in the mixture density and molecular weight, which might be worth investigating.

To get a better understanding of the particle-wall restitution coefficients and models, these can be tested for a 90 degree pipe bend to investigate if the rebound models result in higher overall erosion rates in comparison with the case when the restitution coefficient was 1.0. If the rebound models do not lead to higher overall erosion rates than for the case when the restitution coefficient is 1.0, it could be due to the complexity of the geometry where it is challenging to predict the outcome. Another possibility could be that the mesh is too coarse near the walls, which may result in higher particle velocity after impact with the wall, that is, in higher erosion rates. By using a finer grid, the rebound velocity would become more accurate. However, the particles have to be smaller than the cells in order for the Lagrangian method to compute accurate results.

Appendix A

Models and solvers

Here the selected models and solvers inside the STAR-CCM+ program are given for both the continuous and the dispersed phase.

Table A.1: Physical models and solvers in STAR-CCM+ used for continuous phase modeling

Models selected for the continuous phase
Cell Quality Remediation
Exact Wall Distance
Gas
Gradients
$k - \varepsilon$ Turbulence
Lagrangian Multiphase
Real Gas
Realizable $k - \varepsilon$ Two-Layer
Reynolds-Averaged Navier-Stokes
Segregated Flow
Segregated Fluid Enthalpy
Steady
Three Dimensional
Turbulent
Two-Layer All y+ Wall Treatment
Van der Waals

Table A.2: Physical models and solvers in STAR-CCM+ used for dispersed phase modeling

Models selected for the dispersed phase
Constant Density
Drag Force
Erosion
Material Particles
Pressure Gradient Force
Residence Time
Solid
Spherical Particles
Track File
Virtual Mass

Appendix B

Overall erosion results

Here are the results from the overall erosion rate calculated by the STAR-CCM+ program for different particle sizes, erosion models, particle-wall rebound models, and rebound coefficients. Table B.1 shows the results from Fig. 5.7, 5.8 and 5.9

Table B.1: Overall erosion rate for Oka et al. with Forder et al. rebound model

Label	**Particle size**	**Overall ER**
a	$4.00 \cdot 10^{-7}$ m	$9.38 \cdot 10^{-14}$ g/hr
b	$4.00 \cdot 10^{-6}$ m	$3.68 \cdot 10^{-11}$ g/hr
c	$4.00 \cdot 10^{-5}$ m	$2.39 \cdot 10^{-7}$ g/hr
d	$1.00 \cdot 10^{-4}$ m	$4.02 \cdot 10^{-6}$ g/hr
e	$1.50 \cdot 10^{-4}$ m	$2.19 \cdot 10^{-5}$ g/hr
f	$2.50 \cdot 10^{-4}$ m	$8.16 \cdot 10^{-5}$ g/hr
g	$4.00 \cdot 10^{-4}$ m	$3.17 \cdot 10^{-4}$ g/hr

Table B.2: Overall erosion rate for Oka et al. with Grant and Tabakoff rebound model

Label	**Particle size**	**Overall ER**
a	$4.00 \cdot 10^{-7}$ m	$9.59 \cdot 10^{-14}$ g/hr
b	$4.00 \cdot 10^{-6}$ m	$3.90 \cdot 10^{-11}$ g/hr
c	$4.00 \cdot 10^{-5}$ m	$2.32 \cdot 10^{-7}$ g/hr
d	$1.00 \cdot 10^{-4}$ m	$4.39 \cdot 10^{-6}$ g/hr
e	$1.50 \cdot 10^{-4}$ m	$2.22 \cdot 10^{-5}$ g/hr
f	$2.50 \cdot 10^{-4}$ m	$9.65 \cdot 10^{-5}$ g/hr
g	$4.00 \cdot 10^{-4}$ m	$3.82 \cdot 10^{-4}$ g/hr

Table B.3: Overall erosion rate for DNV with Forder et al. rebound model

Label	**Particle size**	**Overall ER**
a	$4.00 \cdot 10^{-7}$ m	$3.28 \cdot 10^{-13}$ g/hr
b	$4.00 \cdot 10^{-6}$ m	$8.49 \cdot 10^{-11}$ g/hr
c	$4.00 \cdot 10^{-5}$ m	$2.25 \cdot 10^{-7}$ g/hr
d	$1.00 \cdot 10^{-4}$ m	$4.71 \cdot 10^{-6}$ g/hr
e	$1.50 \cdot 10^{-4}$ m	$2.29 \cdot 10^{-5}$ g/hr
f	$2.50 \cdot 10^{-4}$ m	$7.14 \cdot 10^{-5}$ g/hr
g	$4.00 \cdot 10^{-4}$ m	$2.95 \cdot 10^{-4}$ g/hr

Table B.4: Overall erosion rate for DNV with Grant and Tabakoff rebound model

Label	**Particle size**	**Overall ER**
a	$4.00 \cdot 10^{-7}$ m	$3.41 \cdot 10^{-13}$ g/hr
b	$4.00 \cdot 10^{-6}$ m	$9.02 \cdot 10^{-11}$ g/hr
c	$4.00 \cdot 10^{-5}$ m	$2.18 \cdot 10^{-7}$ g/hr
d	$1.00 \cdot 10^{-4}$ m	$4.96 \cdot 10^{-6}$ g/hr
e	$1.50 \cdot 10^{-4}$ m	$2.38 \cdot 10^{-5}$ g/hr
f	$2.50 \cdot 10^{-4}$ m	$8.85 \cdot 10^{-5}$ g/hr
g	$4.00 \cdot 10^{-4}$ m	$2.98 \cdot 10^{-4}$ g/hr

Table B.5: Overall erosion rate for Oka et al. erosion model with constant rebound model

Rebound coeff.	**Particle size**	**Overall ER**
1.0	$1.00 \cdot 10^{-4}$ m	$3.81 \cdot 10^{-6}$ g/hr
1.0	$1.50 \cdot 10^{-4}$ m	$1.84 \cdot 10^{-5}$ g/hr
1.0	$2.50 \cdot 10^{-4}$ m	$8.28 \cdot 10^{-5}$ g/hr
0.9	$1.00 \cdot 10^{-4}$ m	$3.86 \cdot 10^{-6}$ g/hr
0.9	$1.50 \cdot 10^{-4}$ m	$1.74 \cdot 10^{-5}$ g/hr
0.9	$2.50 \cdot 10^{-4}$ m	$7.67 \cdot 10^{-5}$ g/hr
0.8	$1.00 \cdot 10^{-4}$ m	$4.19 \cdot 10^{-6}$ g/hr
0.8	$1.50 \cdot 10^{-4}$ m	$1.71 \cdot 10^{-5}$ g/hr
0.8	$2.50 \cdot 10^{-4}$ m	$7.37 \cdot 10^{-5}$ g/hr

Table B.6: Overall erosion rate for Oka et al. erosion model with constant mass flow rate $1.74 \cdot 10^{-5}$ kg/s

Particle size	**Particle volume**	**Particle mass**	**Overall ER**
$4.00 \cdot 10^{-7}$ m	$1.34 \cdot 10^{-19}$ m^3	$3.48 \cdot 10^{-16}$ kg	$3.75 \cdot 10^{-4}$ g/hr
$4.00 \cdot 10^{-6}$ m	$1.34 \cdot 10^{-16}$ m^3	$3.48 \cdot 10^{-13}$ kg	$1.47 \cdot 10^{-4}$ g/hr
$4.00 \cdot 10^{-5}$ m	$1.34 \cdot 10^{-13}$ m^3	$3.48 \cdot 10^{-10}$ kg	$9.55 \cdot 10^{-4}$ g/hr
$1.00 \cdot 10^{-4}$ m	$2.09 \cdot 10^{-12}$ m^3	$5.44 \cdot 10^{-9}$ kg	$1.03 \cdot 10^{-3}$ g/hr
$1.50 \cdot 10^{-4}$ m	$7.07 \cdot 10^{-12}$ m^3	$1.84 \cdot 10^{-8}$ kg	$1.66 \cdot 10^{-3}$ g/hr
$2.50 \cdot 10^{-4}$ m	$3.27 \cdot 10^{-11}$ m^3	$8.50 \cdot 10^{-8}$ kg	$1.33 \cdot 10^{-3}$ g/hr
$4.00 \cdot 10^{-4}$ m	$1.34 \cdot 10^{-10}$ m^3	$3.48 \cdot 10^{-7}$ kg	$1.48 \cdot 10^{-3}$ g/hr
$7.00 \cdot 10^{-4}$ m	$7.18 \cdot 10^{-10}$ m^3	$1.87 \cdot 10^{-6}$ kg	$1.85 \cdot 10^{-3}$ g/hr
$1.00 \cdot 10^{-3}$ m	$2.09 \cdot 10^{-9}$ m^3	$5.44 \cdot 10^{-6}$ kg	$2.30 \cdot 10^{-3}$ g/hr

Appendix C

Analytical pressure calculations

Under is Table C.1, where the analytical pressure loss was calculated for different initial pressure and temperature.

Table C.1: Analytically calculated pressure loss

Temp [C]	**Pressure [bar]**	**Re**	$\mathbf{h}_f$ **[m^2/s^2]**	ΔP **[bar]**
20	1	$6.34 \cdot 10^4$	26 727.95	0.1753
110	1	$5.91 \cdot 10^4$	62 307.35	0.3140
110	5	$2.81 \cdot 10^5$	60 787.23	1.520
110	10	$5.49 \cdot 10^5$	60 436.44	3.058
110	50	$2.13 \cdot 10^6$	59 500.98	15.23
110	100	$3.38 \cdot 10^6$	59 267.12	31.18
110	175	$3.74 \cdot 10^6$	59 150.19	48.23

Bibliography

[1] GL DNV. "Recommended Practice–DNVGL-RP-O501–Managing Sand Production and Erosion". In: *DNV GL* (2015), pp. 3–60.

[2] F. Leopold and L.M. Rinde. Private communication. 2018.

[3] J.D. Anderson and J. Wendt. *Computational fluid dynamics*. Vol. 206. Springer, 1995.

[4] W.L. McCabe, J.C. Smith, and P. Harriott. *Unit operations of chemical engineering*. Vol. 1130. McGraw-hill New York, 1993, pp. 68–129.

[5] STAR-CCM+. *STAR-CCM+ User guide*. URL: `file:///C:/Program%20Files/CD-adapco/12.02.010-R8/STAR-CCM+12.02.010-R8/doc/en/online/index.html#page/connect%2Fsplash.html`. (accessed: 09.01.2019).

[6] O. Reynolds. "O. Reynolds, Philos. Trans. R. Soc. London 174, 935 (1883)." In: *Philos. Trans. R. Soc. London* 174 (1883), p. 935.

[7] L.B. Timothy. "Laser Doppler Velocimeter Measurements for Validation of Turbulence Modeling in Choke Geometries (Master of Science thesis)". In: *The University of Tulsa, Tulsa, OK* (1999).

[8] R.M. Felder and R.W. Rousseau. *Elementary principles of chemical processes*. Wiley NY etc., 1986.

[9] M. Parsi K. Najmi F. Najafifard S. Hassani B.S. McLaury and S.A. Shirazi. "A comprehensive review of solid particle erosion modeling for oil and gas wells and pipelines applications". In: *Journal of Natural Gas Science and Engineering* 21 (2014), pp. 850–873.

[10] J.D. Schwarzkopf M. Sommerfeld C.T. Crowe and Y. Tsuji. *Multiphase flows with droplets and particles*. CRC press, 2011.

[11] B.E. Lee, J.Y. Tu, and C.A.J. Fletcher. "On numerical modeling of particle–wall impaction in relation to erosion prediction: Eulerian versus Lagrangian method". In: *Wear* 252.3-4 (2002), pp. 179–188.

[12] R. Courant, K. Friedrichs, and H. Lewy. "On the partial difference equations of mathematical physics". In: *IBM journal of Research and Development* 11.2 (1967), pp. 215–234.

[13] L.F. Moody. "Friction factors for pipe flow". In: *Trans. Asme* 66 (1944), p. 672.

[14] R.H. Perry and D.W. Green. *Perry's Chemical Engineers' Handbook/edición Don W. Green y Robert H. Perry*. C 660.28 P47 2008. 1997.

[15] J. Salik, D. Buckley, and W.A. Brainard. "The effect of mechanical surface and heat treatments on the erosion resistance of 6061 aluminum alloy". In: *Wear* 65.3 (1981), pp. 351–358.

[16] A.V. Levy and P. Chik. "The effects of erodent composition and shape on the erosion of steel". In: *Wear* 89.2 (1983), pp. 151–162.

[17] I.M. Hutchings, R.E. Winter, and J.E. Field. "Solid particle erosion of metals: the removal of surface material by spherical projectiles". In: *Proc. R. Soc. Lond. A* 348.1654 (1976), pp. 379–392.

[18] H. Arabnejad S.A. Shirazi B.S. McLaury H.J. Subramani and L.D. Rhyne. "The effect of erodent particle hardness on the erosion of stainless steel". In: *Wear* 332 (2015), pp. 1098–1103.
[19] G.P. Tilly. "A two stage mechanism of ductile erosion". In: *Wear* 23.1 (1973), pp. 87–96.
[20] B.K. Gandhi and S.V. Borse. "Effects of particle size and size distribution on estimating erosion wear of cast iron in sand-water slurries". In: (2002).
[21] A. Elkholy. "Prediction of abrasion wear for slurry pump materials". In: *Wear* 84.1 (1983), pp. 39–49.
[22] H.M.I. Clark. "On the impact rate and impact energy of particles in a slurry pot erosion tester". In: *Wear* 147.1 (1991), pp. 165–183.
[23] G.R. Desale, B.K. Gandhi, and S.C. Jain. "Particle size effects on the slurry erosion of aluminium alloy (AA 6063)". In: *Wear* 266.11-12 (2009), pp. 1066–1071.
[24] Y.I. Oka, K. Okamura, and T. Yoshida. "Practical estimation of erosion damage caused by solid particle impact: Part 1: Effects of impact parameters on a predictive equation". In: *Wear* 259.1-6 (2005), pp. 95–101.
[25] Y.I. Oka and T. Yoshida. "Practical estimation of erosion damage caused by solid particle impact: Part 2: Mechanical properties of materials directly associated with erosion damage". In: *Wear* 259.1-6 (2005), pp. 102–109.
[26] S. Wada and N. Watanabe. "Solid Particle Erosion of Brittle Materials. III. The Interaction with Material Properties of Target and That of Impingement Particle on Erosive Wear Mechanism". In: *Yogyo-Kyokai-Shi(J. Ceram. Soc. Jpn.)* 95.6 (1987), pp. 573–578.
[27] P.H. Shipway and I.M. Hutchings. "The role of particle properties in the erosion of brittle materials". In: *Wear* 193.1 (1996), pp. 105–113.
[28] J.O. Hinze. "Turbulent fluid and particle interaction". In: *Proceedings of the International Symposium on Two-Phase Systems*. Elsevier. 1972, pp. 433–452.
[29] J.A.C. Humphrey. "Fundamentals of fluid motion in erosion by solid particle impact". In: *International journal of heat and fluid flow* 11.3 (1990), pp. 170–195.
[30] F. Iain, J. Wolak, and Y. Kabil. "Erosion of Metals by Solid Par-ticles". In: *ASTM j Mater* 2 (1967), p. 682.
[31] A. Levy and G. Hickey. "Surface degradation of metals in simulated synthetic fuels plant environments". In: (1981).
[32] T. Foley and A. Levy. "The erosion of heat-treated steels". In: *Wear* 91.1 (1983), pp. 45–64.
[33] C.E. Smeltzer, M.E. Gulden, and W.A. Compton. "Mechanisms of metal removal by impacting dust particles". In: *Journal of basic engineering* 92.3 (1970), pp. 639–652.
[34] A.J. Burnett, S.R. De Silva, and A.R. Reed. "Comparisons between "sand blast" and "centripetal effect accelerator" type erosion testers". In: *Wear* 186 (1995), pp. 168–178.
[35] G. Grant and W. Tabakoff. "Erosion prediction in turbomachinery resulting from environmental solid particles". In: *Journal of Aircraft* 12.5 (1975), pp. 471–478.
[36] A. Forder, M. Thew, and D. Harrison. "A numerical investigation of solid particle erosion experienced within oilfield control valves". In: *Wear* 216.2 (1998), pp. 184–193.
[37] A.V. Levy. "The role of plasticity in erosion". In: *International Conference on Erosion by Liquid and Solid Impact, 5 th, Cambridge, England*. 1979, pp. 39–41.
[38] R. Brown, E.J. Jun, and J.W. Edington. "Erosion of α-Fe by spherical glass particles". In: *Wear* 70.3 (1981), pp. 347–363.
[39] T. Deng A.R. Chaudhry M. Patel I. Hutchings and M.S.A. Bradley. "Effect of particle concentration on erosion rate of mild steel bends in a pneumatic conveyor". In: *Wear* 258.1-4 (2005), pp. 480–487.
[40] K. Haugen O. Kvernvold A. Ronold and R. Sandberg. "Sand erosion of wear-resistant materials: Erosion in choke valves". In: *Wear* 186 (1995), pp. 179–188.

[41] W. Tabakoff, R. Kotwal, and A. Hamed. "Erosion study of different materials affected by coal ash particles". In: *Wear* 52.1 (1979), pp. 161–173.
[42] K.R. Ahlert. "Effects of particle impingement angle and surface wetting on solid particle erosion of AISI 1018 steel". PhD thesis. BUniversity of Tulsa, 1994.
[43] B.S. McLaury S.A. Shirazi J.R. Shadley and F. Rybicki. "Modeling erosion in chokes". In: *ASME-PUBLICATIONS-FED* 236 (1996), pp. 773–782.
[44] J.H. Neilson and A. Gilchrist. "Erosion by a stream of solid particles". In: *wear* 11.2 (1968), pp. 111–122.
[45] M.S. Wallace J.S. Peters T.J. Scanlon W.M. Dempster S. McCulloch and J.B. Ogilvie. "CFD-based erosion modeling of multi-orifice choke valves". In: *Proceedings of 2000 ASME fluids engineering summer meeting*. 2000.
[46] J.F. Archard and W. Hirst. "The wear of metals under unlubricated conditions". In: *Proc. R. Soc. Lond. A* 236.1206 (1956), pp. 397–410.
[47] R.E. Vieira A. Mansouri B.S. McLaury and S.A. Shirazi. "Experimental and computational study of erosion in elbows due to sand particles in air flow". In: *Powder technology* 288 (2016), pp. 339–353.
[48] Y. Zhang E.P. Reuterfors B.S. McLaury S.A. Shirazi and E.F. Rybicki. "Comparison of computed and measured particle velocities and erosion in water and air flows". In: *Wear* 263.1-6 (2007), pp. 330–338.
[49] R. Zhang and H. Liu. "Numerical simulation of solid particle erosion in a 90 degree bend for gas flow". In: *ASME 2014 33rd International Conference on Ocean, Offshore and Arctic Engineering*. American Society of Mechanical Engineers. 2014, V06AT04A044–V06AT04A044.
[50] A.T. Bourgoyne Jr. "Experimental study of erosion in diverter systems due to sand production". In: *SPE/IADC Drilling Conference*. Society of Petroleum Engineers. 1989.
[51] T. Evans H. Bennett Y. Sun J. Alvarez E. Babaian-Kibala and J.W. Martin. "Studies of inhibition and monitoring of metal loss in gas systems containing solids". In: *CORROSION 2004*. NACE International. 2004.
[52] M.N. Pyboyina. "Experimental investigation and computational fluid dynamics simulations of erosion on electrical resistance probes". PhD thesis. University of Tulsa, 2006.
[53] M. Parsi M. Agrawal V. Srinivasan R.E. Vieira C.F. Torres B.S. McLaury and S.A. Shirazi. "CFD simulation of sand particle erosion in gas-dominant multiphase flow". In: *Journal of Natural Gas Science and Engineering* 27 (2015), pp. 706–718.
[54] M. Parsi R.E. Vieira N. Kesana B.S. McLaury and S.A. Shirazi. "Ultrasonic measurements of sand particle erosion in gas dominant multiphase churn flow in vertical pipes". In: *Wear* 328 (2015), pp. 401–413.
[55] M. Parsi A. Al-Sarkhi M. Kara P. Sharma B.S. McLaury and S.A. Shirazi. "A new dimensionless number for solid particle erosion in natural gas elbows". In: *Wear* 390 (2017), pp. 80–83.
[56] W. Peng and X. Cao. "Numerical prediction of erosion distributions and solid particle trajectories in elbows for gas–solid flow". In: *Journal of Natural Gas Science and Engineering* 30 (2016), pp. 455–470.
[57] W. Peng and X. Cao. "Numerical simulation of solid particle erosion in pipe bends for liquid–solid flow". In: *Powder technology* 294 (2016), pp. 266–279.
[58] L. Zeng, G.A. Zhang, and X.P. Guo. "Erosion–corrosion at different locations of X65 carbon steel elbow". In: *Corrosion Science* 85 (2014), pp. 318–330.
[59] G.C. Pereira, F.J. de Souza, and D.A. de Moro Martins. "Numerical prediction of the erosion due to particles in elbows". In: *Powder Technology* 261 (2014), pp. 105–117.
[60] X. Chen. "Application of computational fluid dynamics (CFD) to flow simulation and erosion prediction in single-phase and multiphase flow". PhD thesis. University of Tulsa, 2004.

[61] P.G. Kumar B.R.J. Smith D. Vedapuri H.J. Subramani and L.D. Rhyne. “Sand fines erosion in gas pipelines–Experiments and CFD modeling”. In: *CORROSION 2014*. NACE International. 2014.

[62] Schlumberger. *Oilfiel Glossary: choke*. URL: `https://www.glossary.oilfield.slb.com/en/Terms/c/choke.aspx`. (accessed: 20.11.2018).